Journal of Fluids and Structures 48 (2014) 122–155

Contents lists available at ScienceDirect

Journal of Fluids and Structures

journal homepage: www.elsevier.com/locate/jfs

Delamination in sandwich panels due to local water slamming loads

J. Xiao, R.C. Batra *

Department of Engineering Science and Mechanics, M/C 0219, Virginia Polytechnic Institute and State University, Blacksburg, VA 24061, USA

ARTICLE INFO

Article history:
Received 26 March 2013
Accepted 9 February 2014
Available online 20 March 2014

Keywords:
Water entry
Curved sandwich panel
Finite deformations
Delamination

ABSTRACT

We study delamination in a sandwich panel due to transient finite plane strain elastic deformations caused by local water slamming loads and use the boundary element method to analyze motion of water and the finite element method to determine deformations of the panel. The cohesive zone model is used to study delamination initiation and propagation. The fluid is assumed to be incompressible and inviscid, and undergo irrotational motion. A layer-wise third order shear and normal deformable plate/shell theory is employed to simulate deformations of the panel by considering all geometric nonlinearities (i.e., all non-linear terms in strain–displacement relations) and taking the panel material to be St. Venant–Kirchhoff (i.e., the second Piola–Kirchhoff stress tensor is a linear function of the Green–St. Venant strain tensor). The Rayleigh damping is introduced to account for structural damping that reduces oscillations in the pressure acting on the panel/water interface. Results have been computed for water entry of (i) straight and circular sandwich panels made of Hookean materials with and without consideration of delamination failure, and (ii) flat sandwich panels made of the St. Venant–Kirchhoff materials. The face sheets and the core of sandwich panels are made, respectively, of fiber reinforced composites and soft materials. It is found that for the same entry speed (i) the peak pressure for a curved panel is less than that for a straight panel, (ii) the consideration of geometric nonlinearities significantly increases the peak hydrodynamic pressure, (iii) delamination occurs in mode-II, and (iv) the delamination reduces the hydroelastic pressure acting on the panel surface and hence alters deformations of the panel.

1. Introduction

Local water slamming is characterized by large hydrodynamic loads of short duration which can cause significant structural damage, e.g., see Faltinsen (1993). von Karman (1929) studied the water entry of a V-shape wedge of small dead rise angle β by using the conservation of linear (or translational) momentum and the concept of added mass. Subsequently, Wagner (1932) generalized von Kármán's work by including effects of water splash-up on a body with a small deadrise angle β. Sedov (1934) extended Wagner's work to large deadrise angles. Correction factors to Wagner's solution to consider 3-D effects were proposed by Yu (1945). Bisplinghoff and Doherty (1952) conducted 2-D experiments and showed that Wagner's solution overestimated effects of the piled-up water. Zhao et al. (1997) generalized Wagner's solution for arbitrary

* Corresponding author. Tel.: +1 540 231 6051; fax: +1 540 231 4574.
E-mail addresses: xiaojian@vt.edu (J. Xiao), rbatra@vt.edu (R.C. Batra).

http://dx.doi.org/10.1016/j.jfluidstructs.2014.02.008
0889-9746

values of β and numerically solved the problem with the boundary integral method. Effects of jet flow were neglected and computed results were found to agree well with the corresponding experimental findings.

Cointe (1989) used the method of asymptotic expansions and extended Wagner's theory to oblique impacts and initially curved free surfaces. Howison et al. (1991) extended Cointe's work to axisymmetric and 3-D problems. Donguy et al. (2001) used the finite element method (FEM) to analyze fluid–structure interaction (FSI) problems and found that Cointe's and Howison et al.'s solutions over-predict the maximum pressure.

Shiffman and Spencer (1945, 1951) investigated the vertical impact of spheres and cones on water and developed an analytical solution for a cone impacting water at normal incidence. A solution for the linearized problem involving the impact on water of a body at an arbitrary angle was developed by Trilling (1950). Schnitzer and Hathaway (1953) presented an approximate method for computing the water impact loads and pressure distributions on elliptic cylinders during oblique impacts. Mei et al. (1999) analytically and numerically solved 2-D water impact problems for wedges and circular cylinders including effects of jet flow. Korobkin and Khabakhpasheva (2006) have presented a semi-analytical method to study the coupled fluid–structure problem for wedge impact. Miloh (1991a, 1991b) derived expressions of the slamming force for water entry of rigid spheres and showed that results from these formulae agreed well with the available experimental data.

Similarity solutions for water entry of a rigid wedge were developed by Dobrovol'Skaya (1969). Zhao and Faltinsen (1993) validated their numerical solutions obtained with the boundary element method (BEM) by comparing them with the similarity solutions for $4^\circ \le \beta \le 81^\circ$.

The fluid motion in water entry problems has been simulated numerically by using the FEM (Anghileri and Spizzica, 1995; Donguy et al., 2001; Das and Batra, 2011), the FEM with arbitrary Lagrange Euler (ALE) formulation (Stenius et al., 2006), smoothed particle hydrodynamics (SPH) method (Oger et al., 2006), computational fluid dynamics (CFD) solver based on the finite volume method (Piro and Maki, 2013), and the BEM (Battistin and Iafrati, 2003; Lin and Ho, 1994; Zhao and Faltinsen, 1993). Wu et al. (2004) numerically and experimentally investigated the water entry of a freely falling rigid wedge, and introduced an auxiliary function to decouple the hydrodynamic force due to rigid body acceleration. The water entry of a freely falling rigid wedge and considering its rotations has been numerically simulated by Xu et al. (2010). Lin and Ho (1994) used the BEM to study the influence of the water depth on the slamming pressure acting on a rigid wedge. They found that the maximum impact pressure is higher for shallow water than that for deep water which agreed with their experimental observations. Battistin and Iafrati (2003) used the BEM to simulate 2-D water entry problems of arbitrary shaped bodies. Sun (2007) and Sun and Faltinsen (2006, 2009) numerically analyzed water slamming problems for arbitrary geometries using the BEM for studying motion of the water that was modeled as non-viscous and incompressible, and the modal analysis technique for deformations of the cylindrical shell. They considered effects of gravity and flow separation from the solid surface. Piro and Maki (2013) investigated the water entry and exit of flexible bodies using the tightly coupled FSI solver in which the fluid flow is simulated by a CFD solver based on the finite volume method and the structural response by modal analysis.

Yettou et al. (2007) experimentally measured hydrodynamic pressures acting on rigid wedges during their free fall into stationary water and analytically solved the problem. Nila et al. (2012) experimentally studied the water entry of rigid and deformable bodies, and used the high speed Particle Image Velocimetry (PIV) technique to determine fluid flow around immersed bodies. The experimentally found velocity field, except in the spray root region, was found to agree well with the corresponding analytical and numerical results. Panciroli et al. (2012, 2013) experimentally and numerically analyzed the water slamming of linear elastic wedges. The experimental results for different values of the panel thickness, deadrise angle and entry velocity were compared with those obtained by using the SPH formulation in LSDYNA. As pointed out by Oger et al. (2006), 20 million particles are needed to correctly predict the pressure on the wedge. Ray and Batra (2013) investigated dynamic failure of a straight sandwich beam made of an anisotropic Hookean material due to slamming loads.

Review articles (Szebehely, 1959; Szebehely and Basin, 1954) suggest that efforts should be concentrated on non-linear free surface boundary conditions and the hydroelastic aspects of the impact. Abrate (2011) has recently reviewed the literature on water slamming. Seddon and Moatamedi (2006) reviewed the water entry problem with focus on the water landing of spacecraft. Korobkin (2004) has summarized analytical models for water slamming problems and developed mathematical models that included higher order terms in the Bernoulli equation to predict the hydrodynamic pressure distribution. The reader is referred to these review articles for additional references on the water entry problem.

In practical water slamming problems, the panel is curved and deformable. Deformations of the panel affect the motion of the fluid and the hydroelastic pressure acting on the fluid/panel interface. Stenius et al. (2011) used LSDYNA to study hydroelastic effects for deformable panels considering different boundary conditions, impact velocities, deadrise angles, membrane effects and panel materials. Lu et al. (2000) employed coupled BE and FE methods for studying hydroelastic effects with the panel modeled as a Timoshenko beam.

The current interest seems to be in the water entry of sandwich panels because of their higher specific stiffness than that of panels made of homogeneous materials. We note that a typical sandwich structure is composed of stiff face sheets and a flexible core, and the slamming pressure acts on a small region. One should consider transverse normal and transverse shear deformations especially when damage and failure of the composite panel are to be delineated. Experimental results for the failure of deformable sandwich composite panels including core shear, delamination and damage of face sheets due to water slamming have been reported by Charca and Shafiq (2010) and Charca et al. (2009). Water slamming problem for a complex shaped composite hull has been analyzed by van Paepegem et al. (2011) both numerically using ABAQUS and

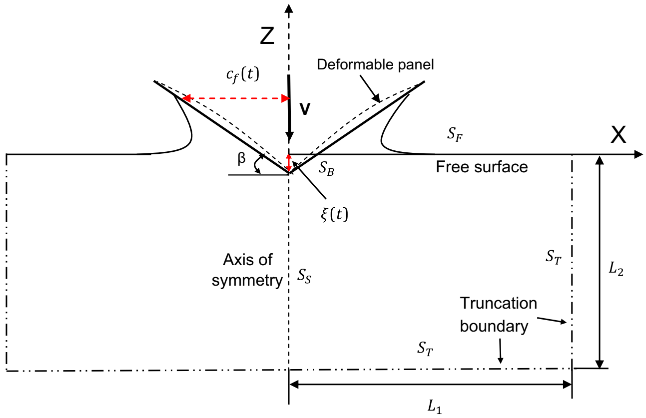

Fig. 1. Schematic sketch of the water slamming problem studied.

experimentally. Hu et al. (2011) approximated the slamming pressure by equivalent bending moment to study delamination of a composite panel using the FE software ANSYS and the cohesive zone model (CZM). Xiao and Batra (2012) studied the motion of the fluid by the BEM and focused on delineating how panel curvature affected the pressure distribution on curved rigid panels. Qin and Batra (2009) studied the hydroelastic problem using the {3, 2}-order plate theory for a sandwich panel of small deadrise angle β and modified Wagner's water impact theory to consider the FSI during slamming. The plate theory incorporates the transverse shear and the transverse normal deformations of the core, but not of the face sheets which were modeled as Kirchhoff plates. Das (2009) and Das and Batra (2011) studied the water slamming of deformable sandwich panels using the commercial FE software LSDYNA with the ALE formulation. They considered all geometric nonlinearities when studying deformations of the panel, assumed the fluid to be compressible, accounted for inertia effects in the fluid and the solid, and examined delamination between the core and the face sheets. They pointed out that boundary conditions at the fluid/panel interface were not well satisfied since the fluid penetrated into the rigid panel. The pressure distribution on the wetted panel surface was found to be oscillatory. Aureli et al. (2010) have exploited deformations of the structure due to FSI to harvest energy.

Here we study delamination of a sandwich panel due to water slamming loads and use coupled BE and FE methods. The BEM is used to analyze motions of the fluid that is modeled as incompressible and inviscid, and whose motions are assumed to be irrotational. This aspect of our work closely follows the work of Lu et al. (2000), Wu (1998), Wu et al. (2004), Wu and Taylor (1996, 2003) and Xu et al. (2010). The coupled BE and FE methods used in the present work are similar to iterative methods discussed by Lu et al. (2000). However, the hydrodynamic pressure evaluation, the jet cut and the FSI methods are different. Furthermore, we use the third order shear and normal deformable plate/shell theory and simulate delamination between the face sheets and the core whereas the Timoshenko theory for a monolithic beam was used by Lu et al. (2000).

We analyze finite transient deformations of a curved sandwich panel by the FEM, employ a third order shear and normal deformable plate/shell theory (TSNDT), account for all geometric nonlinearities, and consider the panel material to be St. Venant–Kirchhoff. Deformations of the panel and the water are coupled by requiring the continuity of the pressure and the normal component of velocity at the water/panel interface. The Rayleigh damping is used to account for damping of the structure that reduces oscillations in the hydrodynamic pressure acting on the water/panel interface. The CZM is incorporated in the TSNDT to study delamination initiation and growth due to water slamming. Thus significant contributions of the work include studying finite deformations of curved sandwich panels, using the TSNDT, and simulating effects of delamination on the hydroelastic response of the panel.

The rest of the paper is organized as follows. In Section 2 we formulate the problem by considering all geometric nonlinearities (i.e., all nonlinear terms in the strain–displacement gradient relations) and coupling between motion of the fluid and deformations of the panel. Numerical methods used to solve the hydroelastic problem are summarized in Section 3. Results for several water slamming problems of deformable sandwich panels and delamination in a sandwich panel are described in Section 4. Conclusions of this work are summarized in Section 5.

2. Formulation of the problem

A schematic sketch of the problem studied is shown in Fig. 1. At time $t=0$, the keel of the ship hull (hereafter referred to as panel) impacts at normal incidence with vertically downward velocity $\boldsymbol{V}$ stationary water occupying the semi-infinite domain $Z \leq 0$ when rectangular Cartesian coordinates (X, Y, Z) fixed to the earth are used to describe motion of the fluid. The positive Z-axis points upwards (i.e., out of water), and the positive Y-axis into the plane of paper. We use curvilinear material coordinates attached to the panel to identify its particles, and simplify the problem by assuming that the panel dimension in the Y-direction is much greater than those in the X- and Z-directions so that a plane strain state of deformation in the XZ-plane can be assumed and the problem can be solved as 2-D. Thus deformations of the panel and the motion of the fluid

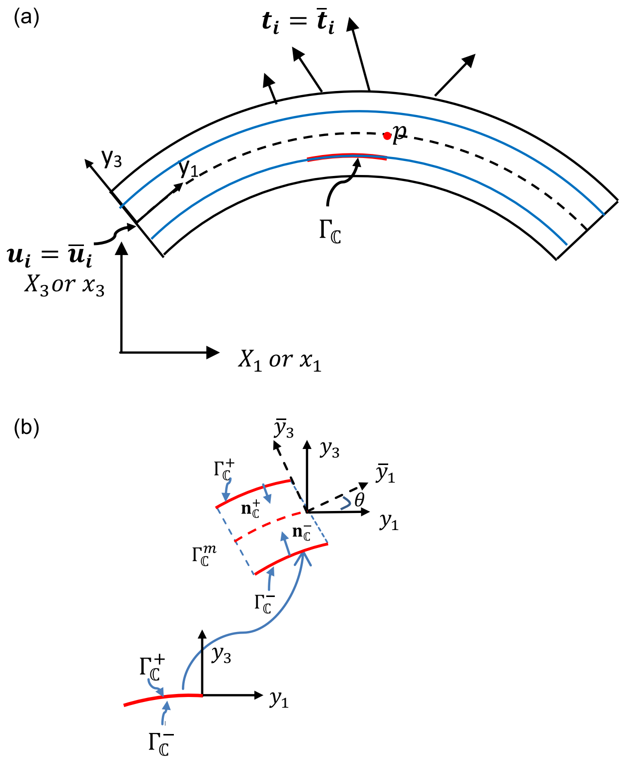

Fig. 2. Schematic sketches of curved beam (a) and of cohesive interface $\Gamma_{\mathbb{C}}$ (b). X_2-, x_2-, y_2- and $\bar{y}_2$-axis pointing into the plane of the paper are not shown in the figure.

are assumed to be independent of the Y-coordinate. Furthermore, we assume that the panel geometry is symmetric about the plane $X=0$ and it initially impacts water along the line $X=Z=0$. Thus motion of water in the region $X \geq 0$ and $Z \leq 0$ and deformations of the right-half of the panel are analyzed.

We note that the hydrodynamic load deforming the panel is highly localized. Thus the slamming problem is idealized as that of a deformable sandwich wedge entering water with a uniform vertically downward velocity (see Fig. 1). We derive equations governing finite deformations of the panel and motion of the water from balance (or conservation) laws of mass, linear (or translational) momentum and moment of momentum (or angular momentum), the strain–displacement relations that include all non-linear terms appropriate for finite deformations, and the relevant constitutive relations. Additional sources of nonlinearity include the *a priori* unknown length of the wetted surface which is a nonlinear function of deformations of the panel, and the deformed shape of the free surface of water. These are to be determined as a part of the solution of the problem.

2.1. Equations governing motion of the fluid

For a 1-m long panel entering stationary water at 10 m/s, Reynolds number equals about 10^7, and viscous effects can be neglected (Batchelor, 1967). Here we also ignore gravitational effects. Furthermore, we assume the water to be incompressible and the motion of water to be irrotational. The assumption of null vorticity implies that there exists a velocity potential φ such that velocity $\boldsymbol{v} = -\nabla\varphi$, where ∇ is the spatial gradient operator in the XZ-plane. The conservation of mass requires that φ satisfy the Laplace equation:

$$\frac{\partial^2\varphi}{\partial Z^2} + \frac{\partial^2\varphi}{\partial X^2} = 0 \quad \text{in the water domain.} \tag{1}$$

In the absence of gravitational force, the balance of linear (translational) momentum for an inviscid fluid requires that

$$\rho\frac{D\boldsymbol{v}}{Dt} = -\nabla p, \tag{2}$$

where ρ is the mass density of water, D/Dt the total time derivative, and the hydrostatic pressure p is determined by solving Eq. (2) under the following boundary conditions:

$$p = p_a, \quad \frac{DX}{Dt} = -\frac{\partial\varphi}{\partial X}, \quad \frac{DZ}{Dt} = -\frac{\partial\varphi}{\partial Z}, \quad \frac{D\varphi}{Dt} = -\frac{1}{2}|\nabla\varphi|^2 \text{ on the free surface of water,} \tag{3a}$$

$$|\boldsymbol{v}| \to 0 \text{ as } (X^2+Z^2)^{1/2} \to \infty \text{ for } X>0 \text{ and } Z \le 0, \tag{3b}$$

$$\frac{\partial \varphi}{\partial X} = 0 \text{ on } X=0. \tag{3c}$$

Here p_a is the atmospheric pressure. In writing boundary condition (3a) we have tacitly neglected the surface tension effect. These equations imply that the velocity of a point on the free surface equals that of the fluid particle instantaneously occupying it. Eq. $(3a)_4$ following from Eq. $(3.a)_1$ and the Bernoulli Eq. (5) given below is used to update the function on the free surface after every time step. Ideally one should specify in Eq. (3b) the rate of decay of the speed of water at infinity. However, we do not do so since the domain occupied by the fluid will be truncated to a finite one when numerically solving the problem. The boundary condition (3c) follows from the assumption that the motion is symmetric about the plane $X=0$. At the fluid/panel interface the non-inter-penetration condition is satisfied if

$$\frac{\partial \varphi}{\partial n} = -\dot{\boldsymbol{U}} \cdot \boldsymbol{n}. \tag{4}$$

Here $\boldsymbol{U}$ and $\dot{\boldsymbol{U}}$ equal, respectively, the displacement and the velocity of a particle of the panel, and $\boldsymbol{n}$ is a unit vector normal to the fluid/panel interface and pointing into the panel.

Recalling that $\boldsymbol{v} = -\nabla\varphi$, Eq. (2) is integrated to give the following Bernoulli equation:

$$p - p_a = -\rho\left(-\frac{\partial \varphi}{\partial t} + \frac{1}{2}|\nabla\varphi|^2\right). \tag{5}$$

2.2. Equations governing deformations of sandwich panel

2.2.1. Strain–displacement gradients relations

Because of the assumption of plane strain deformations we model the panel as a 2-D curved beam schematically shown in Fig. 2. In the reference configuration, we describe the position of a material point p by using orthogonal curvilinear coordinate axes y_1, y_2, y_3 with the y_1-axis along the tangent to the mid-surface of the beam, the y_2-axis pointing into the plane of the paper, and the y_3-axis pointing along the local thickness direction. The coordinate axes y_1, y_2, y_3 move with the downward instantaneous velocity $\boldsymbol{V}$ (rigid translation, no rotation). Let position vectors, with respect to fixed rectangular Cartesian coordinate axes, of point p in the current and the reference configurations be $\boldsymbol{x}$ and $\boldsymbol{X}$, respectively. The y_2-axis is parallel to the x_2- (or the y-) and X_2- (or the Y-) axes. The displacement $\boldsymbol{U}$ of point p is given by

$$\boldsymbol{U} = \boldsymbol{u} + \boldsymbol{u}' = \boldsymbol{x} - \boldsymbol{X}, \tag{6}$$

where $\boldsymbol{u}'$ is the displacement of the origin of the curvilinear coordinate axes y_1, y_2, y_3 and is only a function of time t, and $\boldsymbol{u}$ is the displacement relative to the coordinate axes y_1, y_2, y_3. The displacement, the velocity and the acceleration of point p relative to axes y_1, y_2, y_3 are hereafter called relative or the vibrational displacement, velocity and acceleration, respectively. The translational velocity and acceleration of the origin of the curvilinear coordinate axes y_1, y_2, y_3 are $\boldsymbol{V}$ and $\dot{\boldsymbol{V}}$, respectively.

Components, G_{ij}, of the metric tensor in the reference configuration are given by

$$G_{ij} = \boldsymbol{A}_i \cdot \boldsymbol{A}_j, \quad \boldsymbol{A}_i = \frac{\partial \boldsymbol{X}}{\partial y_i}. \tag{7}$$

For orthogonal curvilinear coordinate axes G_{ij} is non-zero only when $i=j$. We set

$$H_1 = \sqrt{G_{11}}, \quad H_2 = \sqrt{G_{22}} = 1, \quad H_3 = \sqrt{G_{33}} = 1, \quad \tilde{\boldsymbol{e}}_i = \frac{\boldsymbol{A}_i}{H_{(i)}} \text{ (no sum on } i). \tag{8}$$

The ordered set $(\tilde{\boldsymbol{e}}_1, \tilde{\boldsymbol{e}}_2, \tilde{\boldsymbol{e}}_3)$ form orthonormal base vectors for the curvilinear coordinate axes in the reference configuration. We note that

$$H_1 = \left(1 + \frac{y_3}{R}\right), \quad \frac{\partial \tilde{\boldsymbol{e}}_1}{\partial y_1} = -\frac{\tilde{\boldsymbol{e}}_3}{R}, \quad \frac{\partial \tilde{\boldsymbol{e}}_3}{\partial y_1} = \frac{\tilde{\boldsymbol{e}}_1}{R}, \tag{9}$$

where R is the radius of curvature of the point $(y_1, y_2, 0)$ on the mid-surface of the beam.

Physical components of the deformation gradient, $\boldsymbol{F}$, are given by

$$[F] = \begin{bmatrix} 1 + \frac{1}{H_1}\left(\frac{\partial u_1}{\partial y_1} + \frac{u_3}{R}\right) & 0 & \frac{\partial u_1}{\partial y_3} \\ 0 & 1 & 0 \\ \frac{1}{H_1}\left(\frac{\partial u_3}{\partial y_1} - \frac{u_1}{R}\right) & 0 & 1 + \frac{\partial u_3}{\partial y_3} \end{bmatrix}. \tag{10}$$

The Green–St. Venant strain tensor, $\boldsymbol{E}$, defined by

$$\boldsymbol{E} = \frac{1}{2}(\boldsymbol{F}^T\boldsymbol{F} - 1), \tag{11}$$

where **1** is the identity tensor, has the following non-zero physical components:

$$
\begin{aligned}
E_{11} &= \frac{1}{H_1}\left(\frac{\partial u_1}{\partial y_1}+\frac{u_3}{R}\right)+\frac{1}{2{H_1}^2}\left[\left(\frac{\partial u_1}{\partial y_1}+\frac{u_3}{R}\right)^2+\left(\frac{\partial u_3}{\partial y_1}-\frac{u_1}{R}\right)^2\right],\\
E_{33} &= \frac{\partial u_3}{\partial y_3}+\frac{1}{2}\left[\left(\frac{\partial u_1}{\partial y_3}\right)^2+\left(\frac{\partial u_3}{\partial y_3}\right)^2\right],\\
2E_{13} &= \frac{1}{H_1}\left(\frac{\partial u_3}{\partial y_1}-\frac{u_1}{R}\right)+\frac{\partial u_1}{\partial y_3}+\frac{1}{H_1}\left[\frac{\partial u_3}{\partial y_3}\left(\frac{\partial u_3}{\partial y_1}-\frac{u_1}{R}\right)+\frac{\partial u_1}{\partial y_3}\left(\frac{\partial u_1}{\partial y_1}+\frac{u_3}{R}\right)\right].
\end{aligned}
\tag{12}
$$

We note that $\boldsymbol{E}$ incorporates all nonlinearities including the von Karman nonlinearity, and is valid for finite (or large) deformations of the beam.

2.2.2. Equations of motion

The in-plane displacements (u_1, u_3) of a point are governed by the following equations expressing the balance of linear (or translational) momentum written in the Lagrangian description of motion using physical components $T_{11}, T_{13}, T_{31}, T_{33}$, of the first Piola–Kirchhoff stress tensor $\boldsymbol{T}$ (Saada, 1993).

$$\rho_0 \ddot{u}_1 = \frac{1}{H_1}\frac{\partial T_{11}}{\partial y_1}+\frac{1}{H_1}\frac{\partial (H_1 T_{13})}{\partial y_3}+\frac{1}{H_1 R}T_{31}+f_1, \tag{13a}$$

$$\rho_0 \ddot{u}_3 = \frac{1}{H_1}\frac{\partial T_{31}}{\partial y_1}+\frac{1}{H_1}\frac{\partial (H_1 T_{33})}{\partial y_3}-\frac{1}{H_1 R}T_{11}+f_3, \tag{13b}$$

$$u_i(y_1, y_3, 0) = u_i^0(y_1, y_3), \tag{13c}$$

$$\dot{u}_i(y_1, y_3, 0) = \dot{u}_i^0(y_1, y_3), \tag{13d}$$

$$T_{ij}N_j^t = \overline{t}_i(y_1, y_3, t) \ \text{ on } \Gamma_t, \tag{13e}$$

$$u_i(y_1, y_3, t) = \overline{u}_i(y_1, y_3, t) \ \text{ on } \Gamma_u, \tag{13f}$$

$$T_{ij}N_j^{\mathcal{C}+} = \overline{f}_i^{\mathcal{C}+}, \quad T_{ij}N_j^{\mathcal{C}-} = \overline{f}_i^{\mathcal{C}-} \ \text{ on } \Gamma_{\mathcal{C}}, \tag{13g}$$

$$\overline{f}_1^{\mathcal{C}-} = \widehat{a}(\mathbb{R}_{11}\sigma_t+\mathbb{R}_{31}\sigma_n), \quad \overline{f}_3^{\mathcal{C}-} = \widehat{a}(\mathbb{R}_{13}\sigma_t+\mathbb{R}_{33}\sigma_n), \quad \overline{f}_i^{\mathcal{C}+} = -\overline{f}_i^{\mathcal{C}-} \ \text{ on } \Gamma_{\mathcal{C}}, \tag{13h}$$

$$[\mathbb{R}] = \begin{bmatrix} \cos\theta & 0 & \sin\theta \\ 0 & 1 & 0 \\ -\sin\theta & 0 & \cos\theta \end{bmatrix}. \tag{13i}$$

In Eq. (13) indices i and j equal 1 and 3, a repeated index implies summation over the range of the index, f_1 and f_3 are components of the body force per unit reference volume along the y_1-axis and the y_3-axis, respectively, ρ_0 the mass density in the reference configuration, and $\ddot{u}_i = \partial^2 u_i/\partial t^2$. The initial displacement u_i^0 and the initial velocity $\dot{u}_i^0$ are known functions of y_1 and y_3. $\boldsymbol{N}^t$ is a unit outward normal in the reference configuration at a point on the boundary Γ_t where surface tractions are prescribed as $\overline{t}_i$. On boundary Γ_u, displacements are prescribed as $\overline{u}_i$. $\boldsymbol{N}^{\mathcal{C}\pm}$ is the outward unit normal on the corresponding interface $\Gamma_{\mathcal{C}}^{\pm}$, $\widehat{a}$ equals the area into which a unit surface area in the reference configuration is deformed, $\mathbb{R}_{ij}$ the rotation matrix, θ the angle between the y_1-axis and the $\overline{y}_1$-axis, $\overline{f}_i^{\mathcal{C}\pm}$ the traction on the cohesive interface $\Gamma_{\mathcal{C}}^{\pm}$, and σ_t and σ_n the tangential and the normal tractions, respectively, on the cohesive interface in the current configuration. Surface tractions σ_t and σ_n are related to jumps in displacements on the cohesive interface as discussed in Section 2.2.4. As unit normals at corresponding points on the upper and the lower surfaces of a cohesive interface may not be parallel to each other, we use a mean cohesive interface $\Gamma_{\mathcal{C}}^m$ (see Fig. 2) to find surface tractions and jumps in the tangential and the normal displacements on the cohesive interface. Accordingly, we introduce local coordinate axes $\overline{y}_1$ and $\overline{y}_3$, respectively, along the tangent and the normal to the deformed mean cohesive interface $\Gamma_{\mathcal{C}}^m$. The unit outward normal $\mathbf{n}_{\mathcal{C}}^{\pm}$ on $\Gamma_{\mathcal{C}}^{\pm}$ in the current configuration is found from values of the deformation gradient on the corresponding interface. We assume that the rotation angle θ of the mean cohesive interface $\Gamma_{\mathcal{C}}^m$ equals the average of the rotation angles of unit normals $\mathbf{n}_{\mathcal{C}}^{\pm}$. The deformed area $\widehat{a}$ of the mean cohesive interface $\Gamma_{\mathcal{C}}^m$ is taken equal to the average of areas into which unit areas on $\Gamma_{\mathcal{C}}^+$ and $\Gamma_{\mathcal{C}}^-$ are deformed. We note that tractions on $\Gamma_{\mathcal{C}}^+$ and $\Gamma_{\mathcal{C}}^-$ are equal and opposite.

Using the transformation matrix $\mathbb{R}_{ij}$, the jumps in displacements δ_t and δ_n, of corresponding points on $\Gamma_{\mathcal{C}}^+$ and $\Gamma_{\mathcal{C}}^-$ are given by

$$\delta_t = \mathbb{R}_{1j}(u_j^+(y_1, y_3, t) - u_j^-(y_1, y_3, t)) \text{ on } \Gamma_{\mathcal{C}}, \quad j = 1,\ 3, \tag{14a}$$

$$\delta_n = \mathbb{R}_{3j}(u_j^+(y_1, y_3, t) - u_j^-(y_1, y_3, t)) \text{ on } \Gamma_{\mathcal{C}}, \quad j = 1,\ 3, \tag{14b}$$

where $u_i^+(y_1, y_3, t)$ and $u_i^-(y_1, y_3, t)$ represent, respectively, displacements of a point on Γ_C^+ and Γ_C^- with respect to y_1 and y_3 coordinate axes, and δ_t and δ_n equal jumps in the tangential and the normal displacements of corresponding points on Γ_C^+ and Γ_C^- with respect to $\overline{y}_1$ and $\overline{y}_3$ coordinate axes on the mean cohesive interface Γ_C^m.

Initially the panel is assumed to move with a uniform velocity $\mathbf{V}$ along the negative Z-axis and have null vibrational displacement and velocity, i.e.,

$$\dot{\boldsymbol{u}}(y_1, y_3, 0) = 0, \quad \boldsymbol{u}(y_1, y_3, 0) = 0. \tag{15}$$

We assume that the left and the right edges of the panel are undeformed during the water entry. Thus $u_i(0,\ y_3,\ t) = 0$, $u_i(\mathscr{L},\ y_3,\ t) = 0$, $i = 1,\ 3$, on the left and the right edges of the panel. On the bottom surface $\Gamma_t(t)$ (or $y_3 = y_{3b}$) of the panel that contacts water

$$T_{ij}N_j = p\,\hat{a}n_i(y_1, y_{3b}, 0), \quad \frac{\partial\varphi}{\partial n} = -(\dot{\boldsymbol{u}} + \boldsymbol{V})\cdot\boldsymbol{n}, \tag{16a, b}$$

and

$$T_{ij}N_j = 0 \text{ on } \Gamma_f(t). \tag{17}$$

Here $\Gamma_f(t)$ is the part of the bottom surface of the panel not contacting water and also the entire top surface of the panel, and $\dot{\boldsymbol{u}}$ the vibrational velocity of the wetted panel surface. We note that in Eq. (16), T_{ij} is computed from deformations of the panel and p from motion of the water. Furthermore, $\boldsymbol{N}$ is a unit outward normal at a point on $\Gamma_t(t)$ of the panel in the undeformed configuration, and n_i is the component of the unit normal $\boldsymbol{n}$ to the panel surface in the deformed configuration. We note that $\boldsymbol{n}$ and $\hat{a}$ depend upon deformations of the panel. For an inviscid fluid the tangential surface traction vanishes. Also, the tangential velocities of the fluid and the solid particles instantaneously contacting each other may be different. We note that Eq. (16a,b) implies the continuity of surface tractions and the normal component of velocity on the interface $\Gamma_t(t)$ between the panel and the water, and $\Gamma_t(t)$ is to be determined as a part of the solution of the problem. The continuity of surface tractions on $\Gamma_t(t)$ enables one to solve the FSI problem if $\Gamma_t(t)$ were known. The continuity of the normal component of velocity expressed by Eq. (16b) is needed to find $\Gamma_t(t)$. Should the pressure p at a point on $\Gamma_t(t)$ become tensile, then the fluid cannot be contacting the panel at that point. That is, the fluid separates from the panel at that point and the surfaces become traction free. For problems studied herein, this situation did not arise.

2.2.3. Constitutive relations

We assume that the beam material is St. Venant–Kirchhoff for which the strain energy density, W, is given by

$$W = \frac{1}{2}E_{ij}C_{ijkl}E_{kl}, \quad C_{ijkl} = C_{klij} = C_{jikl}. \tag{18}$$

Here $\boldsymbol{C}$ is the fourth-order elasticity tensor having 21 independent components for a general anisotropic material. The strain energy density for the St. Venant–Kirchhoff material reduces to that of a Hookean material if the finite strain tensor $\boldsymbol{E}$ is replaced in Eq. (18) by the strain tensor for infinitesimal deformations. The material with the strain energy density given by Eq. (18) is often called neo-Hookean. Batra (2006) has compared the response of four elastic materials for which a stress tensor is a linear function of an appropriate strain tensor (e.g., the Cauchy stress tensor is a linear function of the Almansi–Hamel strain tensor).

For a nonlinear elastic material, physical components of the second Piola–Kirchhoff stress tensor $\boldsymbol{S}$ are related to $\boldsymbol{E}$ by

$$S_{ij} = \frac{\partial W}{\partial E_{ij}} = C_{ijkl}E_{kl}. \tag{19}$$

For plane strain deformations of an orthotropic material with the material principal axes coincident with the coordinate axes (y_1, y_2, y_3), Eq. (19) reduces to

$$\begin{Bmatrix} S_{11} \\ S_{33} \\ S_{13} \end{Bmatrix} = \begin{bmatrix} C_{1111} & C_{1133} & 0 \\ C_{3311} & C_{3333} & 0 \\ 0 & 0 & C_{1313} \end{bmatrix} \begin{Bmatrix} E_{11} \\ E_{33} \\ 2E_{13} \end{Bmatrix}, \tag{20a}$$

$$C_{1111} = \frac{1-\nu_{23}\nu_{32}}{E_2E_3\mathcal{D}}, \quad C_{3333} = \frac{1-\nu_{12}\nu_{21}}{E_1E_2\mathcal{D}}, \quad C_{1133} = C_{3311} = \frac{\nu_{31}+\nu_{21}\nu_{32}}{E_2E_3\mathcal{D}}, \quad C_{1313} = G_{13}, \tag{20b}$$

$$\mathcal{D} = \frac{1}{E_1E_2E_3}\begin{vmatrix} 1 & -\nu_{21} & -\nu_{31} \\ -\nu_{12} & 1 & -\nu_{32} \\ -\nu_{13} & -\nu_{23} & 1 \end{vmatrix}. \tag{20c}$$

Here E_1, E_2 and E_3 equal Young's moduli along the y_1-, the y_2- and the y_3-axes, respectively, G_{13} is the shear modulus in the y_1y_3-plane, $\upsilon_{12}, \upsilon_{13}$ and υ_{23} are Poisson's ratios. Usually these quantities are defined for infinitesimal deformations.

Recalling that

$$\boldsymbol{T} = \boldsymbol{FS}, \tag{21}$$

where $\boldsymbol{T}$ is the 1st Piola–Kirchhoff stress tensor, we get

$$\begin{bmatrix} T_{11} & T_{13} \\ T_{31} & T_{33} \end{bmatrix} = \begin{bmatrix} F_{11}S_{11}+F_{13}S_{13} & F_{11}S_{13}+F_{13}S_{33} \\ F_{31}S_{11}+F_{33}S_{13} & F_{31}S_{13}+F_{33}S_{33} \end{bmatrix}. \tag{22}$$

Substitution for $\boldsymbol{F}$ from Eq. (10) into Eq. (22), for $\boldsymbol{E}$ from Eq. (12) into Eq. (20) and the result into Eq. (22) gives expressions for $\boldsymbol{T}$ in terms of gradients of displacements u_1 and u_3 and the four elastic constants C_{1111}, C_{1133}, C_{3333}, and C_{1313}. We note that constitutive relations (19) and (21) are materially objective, i.e., are invariant under a rigid body motion superimposed upon the present configuration.

The true stress or the Cauchy stress, $\boldsymbol{\sigma}$, is related to the 1st Piola–Kirchhoff stress by

$$\boldsymbol{\sigma} = \frac{1}{J}\boldsymbol{T}\boldsymbol{F}^T, \tag{23}$$

where J is the determinant of the deformation gradient $\boldsymbol{F}$. Thus $\boldsymbol{\sigma}$ is a more involved function of the displacement gradients than either $\boldsymbol{T}$ or $\boldsymbol{S}$.

We now substitute in Eq. (13) for the first Piola–Kirchhoff stress $\boldsymbol{T}$, and solve the resulting nonlinear coupled partial differential equations (PDEs) for u_1 and u_3 under the pertinent initial and boundary conditions. These PDEs involve 2nd order derivatives of u_1 and u_3 with respect to y_1, y_3 and time t. Thus C^0 basis functions can be used to numerically solve the boundary value problem for the sandwich panel.

2.2.4. Cohesive zone model

2.2.4.1. Mode-I or mode-II deformations. We first describe the CZM for mode-I and mode-II deformations, and then for mixed-mode deformations. We postulate the traction-separation relations depicted in Fig. 3a and b for mode-I and mode-II deformations, respectively. For relative normal (tangential) displacement $\delta_n(\delta_t)$ of adjoining points on the two sides of the interface less than $\delta_n^0(\delta_t^0)$ corresponding to point A in Fig. 3a (Fig. 3b), the traction–separation relation represented by straight line OA is completely reversible. For monotonically increasing values of $\delta_n(\delta_t)$ greater than $\delta_n^0(\delta_t^0)$ the traction–separation relation is given by straight line AB. For $\delta_n = \delta_n^f(\delta_t = \delta_t^f)$ there is complete separation (sliding) at the interface for mode-I (mode-II) deformations. For mode-I deformations, the separated surfaces are traction free and for mode-II deformations the sliding surfaces are assumed to be smooth or frictionless. Should the relative displacement $\delta_n(\delta_t)$

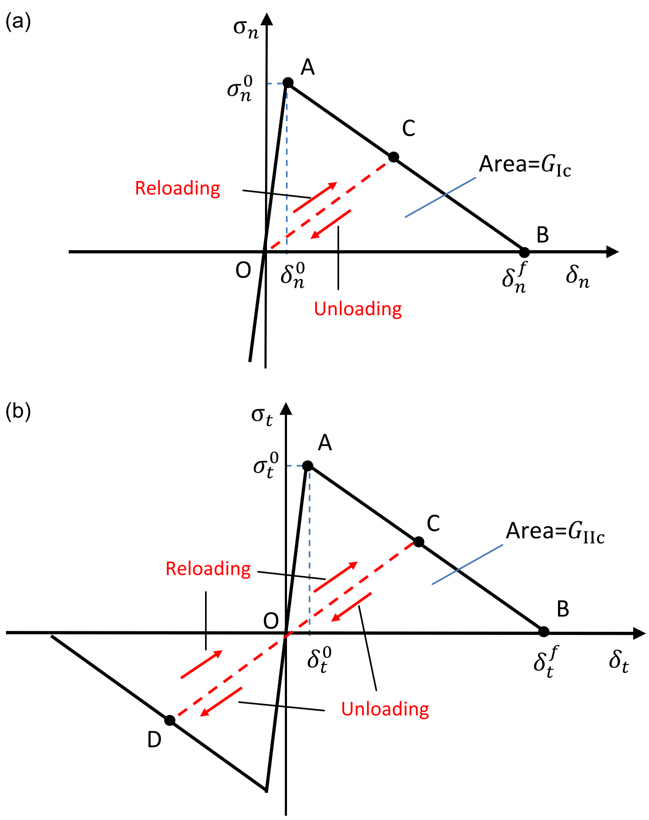

Fig. 3. Traction–separation relations at cohesive interface: (a) mode-I and (b) mode-II.

exceeding $\delta_n^0(\delta_t^0)$ but less than $\delta_n^f(\delta_t^f)$ begin to decrease, then the traction–separation relation follows the path CO for δ_n and COD for δ_t. Upon reversal in the relative displacements, paths OCB and DOCB are followed for δ_n and δ_t, respectively. The area of the triangle OAB equals the critical strain energy release rate (SERR) G_{Ic} (G_{IIc}) for mode-I (mode-II) deformations. Values of G_{Ic} (G_{IIc}) and σ_n^0 (σ_t^0) characterize the interface. Here σ_n^0 (σ_t^0) equals the interface strength for mode-I (mode-II) deformations. The slope, k_s, of straight line OA is estimated. Then

$$\sigma_i = k_s \delta_i, \quad i = t,\ n, \tag{24a}$$

$$\delta_i^0 = \frac{\sigma_i^0}{k_s},\ i = t, n, \tag{24b}$$

and k_s is called the initial stiffness of the interface.

Thus, the delamination initiates when $\sigma_n = \sigma_n^0$ ($\sigma_t = \sigma_t^0$), and complete separation (sliding) occurs when

$$\delta_n^f = \frac{2G_{Ic}}{\sigma_n^0}, \quad \delta_t^f = \frac{2G_{IIc}}{\sigma_t^0}, \tag{25}$$

for pure mode-I (mode-II) deformations.

The interface stiffness k_s should be such that it does not make the system of simultaneous equations to be solved ill-conditioned and effectively prevents interpenetration between two contacting layers when compressive normal traction acts on the interface. For a beam of thickness H we use the relation

$$k_s = \frac{H}{\mathcal{K}} \max(\sigma_n^0, \sigma_t^0), \tag{26}$$

to find k_s, and set the nondimensional parameter $\mathcal{K} = 10^{-9}$.

2.2.4.2. Mixed mode deformations. For mixed-mode deformations, $\delta_n > 0$ and $\delta_t \neq 0$. We follow Camanho and Dávila's (2002) approach, and postulate that the delamination at a point on the interface initiates when

$$\left(\frac{\sigma_n}{\sigma_n^0}\right)^2 + \left(\frac{\sigma_t}{\sigma_t^0}\right)^2 = 1, \tag{27}$$

and complete separation occurs when

$$\left(\frac{G_{\mathrm{I}}}{G_{\mathrm{Ic}}}\right)^2 + \left(\frac{G_{\mathrm{II}}}{G_{\mathrm{IIc}}}\right)^2 = 1. \tag{28}$$

Here σ_n and σ_t are the normal and the tangential tractions on the interface under mixed-mode deformations. Similarly, G_{I} (G_{II}) is the SERR for mode-I (mode-II) deformations for mixed-mode loading.

We define the equivalent mixed-mode relative displacement δ_e by

$$\delta_e = \sqrt{(\delta_t)^2 + (\delta_n)^2} = \frac{\delta_t}{\mu}\sqrt{1+\mu^2} = \delta_n\sqrt{1+\mu^2}, \tag{29}$$

where $\mu\delta_n = \delta_t$, and note that $\mu = 0$ for mode-I, and $\mu \to \infty$ for mode-II deformations.

Assuming that under mixed-mode loading, the interface stiffness for the tangential and the normal traction-separation modes also equals k_s, then substituting for σ_n and σ_t in terms of δ_t and δ_n into Eq. (27), the separation will initiate when

$$\left(\frac{\delta_n}{\sigma_n^0}\right)^2 + \left(\frac{\delta_t}{\sigma_t^0}\right)^2 = \frac{1}{(k_s)^2}, \tag{30}$$

or equivalently,

$$\delta_e^0 = \delta_t^0 \delta_n^0 \sqrt{\frac{1+\mu^2}{(\delta_t^0)^2 + (\mu\delta_n^0)^2}}, \tag{31}$$

where δ_t^0 and δ_n^0 are given by Eq. (24b). We evaluate the mode-mixity ratio μ at every point on the interface and note that it can vary from point to point. However, at a point μ is assumed to stay fixed from separation initiation to separation completion.

In order to find the value δ_e^f of δ_e at complete separation, we assume that the effective traction–effective separation relation under mixed-mode loading is also triangular, i.e., is similar to that for mode-I and mode-II loadings. Thus values of G_{I} and G_{II} at complete separation are given by

$$G_{\mathrm{I}}(1+\mu^2) = \frac{k_s \delta_e^0 \delta_e^f}{2}, \quad G_{\mathrm{II}} = \mu^2 G_{\mathrm{I}}. \tag{32}$$

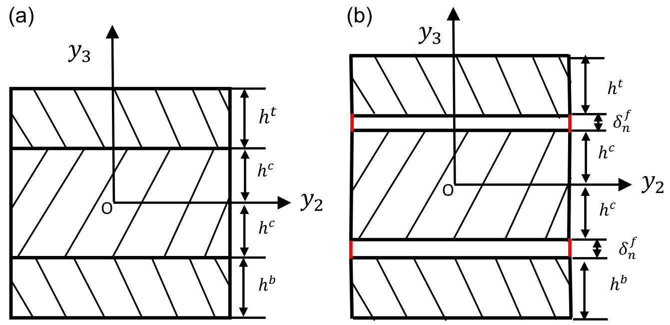

Fig. 4. Cross-section of a 3-layer beam: (a) before delamination and (b) after separation.

Substitution from Eq. (32) into Eq. (28) gives

$$\delta_e^f = \frac{2(1+\mu^2)}{k_s \delta_e^0}\left[\left(\frac{1}{G_{Ic}}\right)^2 + \left(\frac{\mu^2}{G_{IIc}}\right)^2\right]^{-1/2}. \tag{33}$$

Because of the assumption of μ staying constant at a point, should unloading occur for $\delta_e^0 < \delta_e < \delta_e^f$, the unloading curve follows a path similar to the straight line CO in Fig. 3a for mode-I deformations.

2.2.5. Displacement field for the TSNDT

For 2-D problems being studied here, we model the panel as a sandwich beam having three layers and denote displacements of a point in the top, the central, and the bottom layers by superscripts t, c and b, respectively. With the origin of the curvilinear coordinate axes located at the geometric centroid of the rectangular cross-section (e.g., see Fig. 4), we assume the following displacement field in the beam:

$$u_\alpha^c(y_1,y_3,t) = \sum_{i=0}^{3} (y_3)^i u_{\alpha i}^c(y_1,t), \quad \alpha = 1,\ 3, \quad |y_3| \le h^c, \tag{34a}$$

$$u_\alpha^t(y_1,y_3,t) = u_\alpha^c(y_1,h^c,t) + u_{\alpha 0}^t + \sum_{i=1}^{3}\left((y_3)^i - (h^c)^i\right)u_{\alpha i}^t(y_1,t),$$
$$\alpha = 1,\ 3, \quad h^c \le y_3 \le h^c + h^t, \tag{34b}$$

$$u_\alpha^b(y_1,y_3,t) = u_\alpha^c(y_1,-h^c,t) - u_{\alpha 0}^b + \sum_{i=1}^{3}\left((y_3)^i - (-h^c)^i\right)u_{\alpha i}^b(y_1,t),$$
$$\alpha = 1,\ 3, \quad -(h^b+h^c) \le y_3 \le -h^c. \tag{34c}$$

Here u_{10}^c and u_{30}^c are, respectively, the axial and the transverse displacements of a point on the beam mid-surface, $u_{\alpha i}^c$, $u_{\alpha i}^t$ and $u_{\alpha i}^b$ ($\alpha = 1,\ 3,\ \ i = 1,2,3$) may be interpreted as generalized axial and transverse displacements of a point, and $u_{\alpha 0}^t$ and $u_{\alpha 0}^b$ ($\alpha = 1,\ 3$) represent jumps in displacements between adjoining points on the top and the bottom interfaces, respectively, when there is delamination. The top (bottom) interface is between the core and the top (bottom) face sheet. Displacements δ_n and δ_t at the interface between the top layer and the core appearing in Eq. (24a) are related to the displacement field $u_\alpha(y_1,y_3,t)$ by substituting from Eq. (34) into Eq. (14). Thus

$$\delta_t = \mathbb{R}_{1\alpha} u_{\alpha 0}^t, \quad \delta_n = \mathbb{R}_{3\alpha} u_{\alpha 0}^t, \quad \alpha = 1,3, \text{ summed on } \alpha. \tag{35}$$

We are unable to analytically solve the above formulated nonlinear problem. Thus we analyze it numerically.

3. Numerical solution of the problem

3.1. Analysis of motion of the fluid by the boundary element method (BEM)

We use the BEM to solve Laplace Eq. (1) and truncate the domain occupied by the fluid to lengths L_1 and L_2 in the X- and the Z-directions, respectively, as shown in Fig. 1. Values of L_1 and L_2 are determined iteratively till the solution near the panel/water interface has converged within the prescribed tolerance.

Using Green's second identity, the velocity potential at point j in the fluid (either in the interior or on the boundary) can be written as (París and Cañas, 1997)

$$c(j)\varphi(j) = \int_{\partial D} G(\boldsymbol{\xi},j)\frac{\partial \varphi(\xi)}{\partial n}ds(\boldsymbol{\xi}) - \int_{\partial D}\varphi(\boldsymbol{\xi})\frac{\partial G(\xi,j)}{\partial n}ds(\boldsymbol{\xi}), \tag{36}$$

where $(\boldsymbol{\xi},j) = \ln\ r(\boldsymbol{\xi},j)$, $r(\boldsymbol{\xi},j)$ is the distance between source point $\boldsymbol{\xi}$ on the fluid boundary and point j, $c(j)$ is a constant, and D equals the region occupied by the fluid. We note that c, φ, D and $\boldsymbol{n}$ vary with time t; this dependence is not exhibited to simplify the notation. Noting that Eq. (36) holds for a constant velocity potential, we get

$$c(j) = -\int_{\partial D}\frac{\partial G(\xi,j)}{\partial n}ds(\boldsymbol{\xi}). \tag{37}$$

The boundary of the fluid domain is discretized by using 2-node 1-D elements. Integrals in Eq. (36) are numerically evaluated over each element by using 6 Gauss points in each element. Thus Eq. (36) can be written as the following system of coupled simultaneous linear algebraic equations:

$$[H]\begin{Bmatrix}\varphi^F\\ \varphi^B\\ \varphi^{T+S}\end{Bmatrix} = [G]\begin{Bmatrix}\frac{\partial\varphi^F}{\partial n}\\ \frac{\partial\varphi^B}{\partial n}\\ \frac{\partial\varphi^{T+S}}{\partial n}\end{Bmatrix}. \tag{38}$$

In Eq. (38) elements of matrices $[H]$ and $[G]$ depend upon coordinates of nodes, and superscripts F, B, T and S on a quantity represent, respectively, its value at a node on the free surface, the panel, the truncation boundaries and the axis of symmetry.

Recalling that at time t we know at every point on the fluid boundary either φ or $\partial\varphi/\partial n$ we can solve for the other variable at that point. Transforming unknowns in Eq. (38) to the left hand side, we rewrite it as

$$[A]\begin{Bmatrix}\frac{\partial\varphi^F}{\partial n}\\ \varphi^B\\ \varphi^{T+S}\end{Bmatrix} = [B]\begin{Bmatrix}\varphi^F\\ \frac{\partial\varphi^B}{\partial n}\\ \frac{\partial\varphi^{T+S}}{\partial n}\end{Bmatrix}. \tag{39}$$

In writing Eq. (39) we have used boundary condition (4) and taken the velocity of the particles on the panel to be known.

After Eq. (39) has been solved we know φ and $\partial\varphi/\partial n$ at every point on the fluid boundary at time t. Thus the tangential derivative $\partial\varphi/\partial s$ of φ at points on the boundary ∂D can be computed; here s is the arc length along ∂D. The potential function is smoothened, if needed, and the finite difference method is used to evaluate $\partial\varphi/\partial s$. Combining $\partial\varphi/\partial s$ with the computed $\partial\varphi/\partial n$ on ∂D, the vector $\nabla\varphi$ at points on the panel/water interface and on the free surface of water is determined. The free surface profile and values of φ at points on the free surface are updated using Eq. (3a). Eq. (36) is used to determine the velocity potential φ at any point in the fluid domain.

The term $\partial\varphi/\partial t$ needed to determine the pressure field in the fluid domain from Eq. (5) is found by introducing a new variable Ψ defined by

$$\Psi = \frac{\partial\varphi}{\partial t} + \boldsymbol{V}\cdot\nabla\varphi. \tag{40}$$

Recalling that $\boldsymbol{V}$ is a function of time only and φ satisfies Laplace Eq. (1), we conclude that (e.g., see Greco, 2001) Ψ also satisfies the 2-D Laplace equation

$$\frac{\partial^2\Psi}{\partial X^2} + \frac{\partial^2\Psi}{\partial Z^2} = 0. \tag{41}$$

Following Wu (1998) and Sun (2007), boundary conditions for Ψ are

$$\Psi = \boldsymbol{V}\cdot\nabla\varphi + \frac{1}{2}|\nabla\varphi|^2 \quad \text{on the free surface,} \tag{42a}$$

$$\frac{\partial\Psi}{\partial n} = -\boldsymbol{n}\cdot\dot{\boldsymbol{V}} - \boldsymbol{n}\cdot\ddot{\boldsymbol{u}} - \boldsymbol{V}\cdot\nabla(\boldsymbol{n}\cdot\dot{\boldsymbol{u}}) \quad \text{on the fluid/panel interface,} \tag{42b}$$

$$\frac{\partial\Psi}{\partial n} = 0 \text{ on the axis of symmetry and on truncation boundaries.} \tag{42c}$$

Here $\dot{\boldsymbol{V}}$ is the acceleration of the rigid body motion, and $\ddot{\boldsymbol{u}}$ the vibrational acceleration of particles on the panel surface. Substitution for $\partial\varphi/\partial t$ from Eq. (5) into Eq. (40) gives Eq. (42a). Eq. (42c) follows from Eqs. (3c) and (40) because $\boldsymbol{n}=(1,0,0)$ on the axis of symmetry $X=0$, and stays unchanged on truncation boundaries. In deriving Eq. (42b) from Eqs. (4) and (40) we assume that during each infinitesimal time step, Δt, $((\partial/\partial t)+\boldsymbol{V}\cdot\nabla)n = \boldsymbol{0}$. That is, the convective derivative of the unit normal to the panel/water interface in the direction of the rigid translational motion of the panel equals zero. Because of very small time step size used and the iterative procedure adopted to check for convergence of the solution within each time step, the error introduced by this assumption can be controlled within a prescribed tolerance. We note that the unit normal $\boldsymbol{n}$ is updated after every time step Δt. For panels made of rubberlike materials, one will need very small time steps to obtain a converged solution.

At every time t, the boundary value problem defined by Eqs. (41) and (42) is numerically solved by the BEM. The algebraic equation for the determination of Ψ and $\partial\Psi/\partial n$ at boundary points is

$$[A]\begin{Bmatrix} \frac{\partial\Psi^F}{\partial n} \\ \Psi^B \\ \Psi^{T+S} \end{Bmatrix} = [B]\begin{Bmatrix} \Psi^F \\ \frac{\partial\Psi^B}{\partial n} \\ \frac{\partial\Psi^{T+S}}{\partial n} \end{Bmatrix}, \tag{43}$$

where matrices $[A]$ and $[B]$ are the same as those in Eq. (39). Knowing Ψ and φ, from Eq. (39), $\partial\varphi/\partial t$ can be evaluated at all points on the fluid boundary including those on the fluid/panel interface. This approach avoids finding $\partial\varphi/\partial t$ by the backward difference method at the expense of solving Eq. (43). Recall that the value of φ at any point in the fluid domain is found from Eqs. (36) and (37).

3.2. Analysis of the motion of free surface of water

The thickness of the water layer between the free surface and the panel near the terminus of the wetted length of the panel becomes very small and necessitates using extremely small time steps for analyzing subsequent motion of the water in the FSI problem. As explained in Xiao and Batra (2012) for a rigid panel, we cut the thin jet, smoothen the free surface, re-mesh it and derive values of variables at the newly generated nodes by interpolating and extrapolating from those at nodes on the previous mesh. We numerically integrate Eq. (3a) to find the motion of free surface of water.

3.3. Analysis of deformations of the panel by the finite element method

We refer the reader to Batra and Xiao (2013a) for derivation of the governing equations, boundary conditions for the TSNDT, and a weak formulation of the initial-boundary-value problem (IBVP). By introducing the stiffness proportional Rayleigh damping to account for structural damping that reduces high frequency vibrations of the panel, we get the following system of coupled nonlinear ordinary differential equations (ODEs) for finding deformations of the panel:

$$\boldsymbol{M}\ddot{\boldsymbol{d}}+\boldsymbol{C}\dot{\boldsymbol{d}}+\boldsymbol{K}(\boldsymbol{d})\boldsymbol{d}=\boldsymbol{F}^{ext}+\boldsymbol{F}^{c}, \tag{44a}$$

$$\boldsymbol{F}^{ext}=\int_0^{\ell}\left[\Phi\left(y_1,-h^b-h^c\right)\right]^T\begin{Bmatrix} -F_{31} \\ F_{11}\end{Bmatrix}(p-p_a)H_1\,dy_1+\boldsymbol{F}^{rig}, \tag{44b}$$

$$\boldsymbol{F}^{rig}=-\int_{-h^b-h^c}^{h^b+h^c}\int_0^{\mathscr{L}}[\Phi]^T\begin{Bmatrix}\dot V_1 \\ \dot V_3\end{Bmatrix}\rho_0H_1\,dy_1\,dy_3, \tag{44c}$$

$$\begin{aligned}\boldsymbol{F}^{c}=&\int_0^{\mathscr{L}}\left([\Phi(y_1,h^{c-})]-[\Phi(y_1,h^{c+})]\right)^T\begin{Bmatrix}\bar f_1^{\mathcal{C}-} \\ \bar f_3^{\mathcal{C}-}\end{Bmatrix}H_1\,dy_1\\ &+\int_0^{\mathscr{L}}\left([\Phi(y_1,-h^{c-})]-[\Phi(y_1,-h^{c+})]\right)^T\begin{Bmatrix}\bar f_1^{\mathcal{C}-} \\ \bar f_3^{\mathcal{C}-}\end{Bmatrix}H_1\,dy_1,\end{aligned} \tag{44d}$$

$$\boldsymbol{C}=\alpha\boldsymbol{K}(\boldsymbol{d}(0)). \tag{44e}$$

Here $\boldsymbol{M}$ is the mass matrix, $\boldsymbol{C}$ the damping matrix defined by Eq. (44e), α the Rayleigh coefficient, $\boldsymbol{K}(\boldsymbol{d})$ the stiffness matrix, $\boldsymbol{d}$ the vector of generalized displacements of nodes on the centroidal axis of the panel, and ℓ the arc length of the fluid/panel interface in the reference configuration and $\mathscr{L}$ the total are length of the panel. Furthermore, F_{31} and F_{11} are components of the deformation gradient, $[\Phi]$ defined in Eq. (42) of Batra and Xiao (2013a) is the matrix of the FE basis functions, $\boldsymbol{F}^{ext}$ is force vector defined by Eq. (44b) in which the pressure exerted by the fluid on the panel is denoted by p, and p_a is the atmospheric pressure. The integration in Eq. (44b) extends over the fluid/panel interface, and $\boldsymbol{F}^{rig}$ is the inertia force vector due to rigid body acceleration of the panel. The force vector $\boldsymbol{F}^{c}$ represents tractions on the cohesive interface, and $h^{c\pm}$ equals the value of y_3 on $\Gamma_{\mathcal{C}}^{\pm}$. We note that the damping matrix $\boldsymbol{C}$ is assumed to be proportional to the value of the stiffness matrix at time $t=0$.

We first discuss how to find the rigid body motion of the panel, and then vibrational displacements of panel particles. Assuming $V(t)$ is the component of $\boldsymbol{V}$ along the Z-direction and $\dot V(t)$ is the corresponding acceleration, the rigid body acceleration of the panel in the Z-direction can be calculated from

$$M^*\dot V(t)=F_Z-M^*g, \tag{45a}$$

$$F_Z=-M_a^*\dot V+F_Z'. \tag{45b}$$

Here M^* is the total mass of the panel, g the acceleration due to gravity, and F_Z the total upward force due to the hydrodynamic pressure acting on the panel. We note that F_Z is an implicit function of the acceleration of fluid particles contacting the panel. We decompose it into two parts: the upward force $F_Z^{\prime}$ without considering acceleration of fluid particles and $M_a^*\dot{V}$ that depends upon the acceleration of fluid particles abutting the panel. The quantity M_a^*, given by Eq. (51) below, is called the added mass.

The numerical solution may diverge when the added mass M_a^* is greater than the total mass of the body as discussed by Causin et al. (2005). Recall that the water slamming pressure is a function of the acceleration of solid particles on the fluid/panel interface. Wu and Taylor (1996, 2003) and Xu et al. (2010) decoupled the inter-dependence of rigid body acceleration and the fluid force by introducing two auxiliary functions. Young (2007) analyzed the hydroelastic problem for propellers by coupled BE and FE methods and obtained the added mass matrix from the solution of the motion of the fluid by the BEM. We separate the pressure term (e.g, see Eq. (49a)) due to acceleration and calculate the added mass effect for rigid body motion and vibration of the solid body. We used this approach to simulate the free drop into stationary water of a light weight rigid wedge and a rigid ship bow section in Xiao and Batra (2012), and adopt it here to analyze the FSI of deformable panels.

Substituting for $(\partial\Psi/\partial n)^B$ from Eqs. (42b) and (42c) into Eq. (43) we get

$$[A]\left\{\begin{array}{c}\frac{\partial\Psi^F}{\partial n}\\ \Psi^B\\ \Psi^{T+S}\end{array}\right\}=[B]\left\{\begin{array}{c}\Psi^F\\ -\boldsymbol{n}\cdot\ddot{\boldsymbol{u}}-\boldsymbol{n}\cdot\dot{\boldsymbol{V}}-\boldsymbol{n}\cdot\nabla(\boldsymbol{n}\cdot\dot{\boldsymbol{u}})\\ 0\end{array}\right\}. \tag{46}$$

With the notation

$$[\mathbb{Q}]=\begin{bmatrix}\mathbb{Q}_{11} & \mathbb{Q}_{12} & \mathbb{Q}_{13}\\ \mathbb{Q}_{21} & \mathbb{Q}_{22} & \mathbb{Q}_{23}\\ \mathbb{Q}_{31} & \mathbb{Q}_{32} & \mathbb{Q}_{33}\end{bmatrix}=[A]^{-1}[B],$$

we write

$$\begin{aligned}\{\Psi^B\}&=\left[\mathbb{Q}_{21}\quad \mathbb{Q}_{22}\quad \mathbb{Q}_{23}\right]\left\{\begin{array}{c}\Psi^F\\ -\boldsymbol{n}\cdot\ddot{\boldsymbol{u}}-\boldsymbol{n}\cdot\dot{\boldsymbol{V}}-\boldsymbol{n}\cdot\nabla(\boldsymbol{n}\cdot\dot{\boldsymbol{u}})\\ 0\end{array}\right\},\\ &=\{\Psi_1^B\}+\{\Psi_2^B\}+\{\Psi_3^B\},\end{aligned} \tag{47}$$

where

$$\begin{aligned}&\{\Psi_1^B\}=-[\mathbb{Q}_{22}]\{\boldsymbol{n}\cdot\ddot{\boldsymbol{u}}\},\quad \{\Psi_2^B\}=-[\mathbb{Q}_{22}]\{\boldsymbol{n}\cdot\dot{\boldsymbol{V}}\},\\ &\{\Psi_3^B\}=\left[\mathbb{Q}_{21}\quad \mathbb{Q}_{22}\quad \mathbb{Q}_{23}\right]\left\{\begin{array}{c}\Psi^F\\ -\boldsymbol{n}\cdot\nabla(\boldsymbol{n}\cdot\dot{\boldsymbol{u}})\\ 0\end{array}\right\}.\end{aligned} \tag{48}$$

The coefficient matrix $[\mathbb{Q}]$ is derived from matrices A and B appearing in the BE formulation of the fluid problem.

By combining Eqs. (40), (5) and (48), we get following equations for the pressure acting on the panel/fluid interface:

$$p-p_a=-\rho\left(-\Psi^B+\boldsymbol{V}\cdot\nabla\varphi+\frac{1}{2}|\nabla\varphi|^2\right)=p_1+p_2+p_3, \tag{49a}$$

$$p_1=\rho\Psi_1^B=-\rho\left[\overline{\mathbb{Q}}_{22}\right]\{\boldsymbol{n}\cdot\ddot{\boldsymbol{u}}\}=-\rho\left[\overline{\mathbb{Q}}_{22}\right][\mathbb{C}]\ddot{\boldsymbol{d}}, \tag{49b}$$

$$p_2=\rho\Psi_2^B=-\rho\left[\overline{\mathbb{Q}}_{22}\right]\{n_Z\}\dot{\boldsymbol{V}}, \tag{49c}$$

$$p_3=-\rho\left(-\Psi_3^B+\boldsymbol{V}\cdot\nabla\varphi+\frac{1}{2}|\nabla\varphi|^2\right), \tag{49d}$$

$$\overline{\mathbb{Q}}_{22}(j)=\mathbb{Q}_{22}(i,j)\left(\frac{s_{i+1}-s}{s_{i+1}-s_i}\right)+\mathbb{Q}_{22}(i+1,j)\left(\frac{s-s_i}{s_{i+1}-s_i}\right),\quad j=1,2,\ldots,\mathcal{N}. \tag{49e}$$

Here p_1 is the pressure due to vibrational acceleration of the deformable panel, p_2 the pressure due to rigid body acceleration of the panel, p_3 the pressure without considering acceleration due to rigid body motion and vibration of the panel, and $\{n_Z\}$ the component of the unit normal to the fluid/panel interface along the Z-axis with the unit normal pointing out of the fluid. The coefficient matrix $\overline{\mathbb{Q}}_{22}$ for point p between nodes i and $i+1$ is evaluated by using Eq. (49e) in which s, s_i and s_{i+1} are, respectively, the arc length of point p, node i and node $i+1$, and $\mathcal{N}$ equals the number of nodes of the fluid part of the fluid/panel interface. The matrix $[\mathbb{C}]$ transforms the acceleration $\ddot{\boldsymbol{d}}$ in curvilinear coordinates to $\{\boldsymbol{n}\cdot\ddot{\boldsymbol{u}}\}$. We note that nodes for the BE and the FE meshes in the fluid and the solid domains on the fluid/panel interface need not coincide with each other, and we find values of a quantity at the desired location by either interpolating or extrapolating from values at points where they are known.

Integrating component of the pressure in the Z-direction over the fluid/panel interface gives the total Z-force acting on the panel. Thus using Eq. (45b) we get

$$F_Z = \int_0^{\ell} (p_1+p_2+p_3) n_Z H_1 \, dy_1 = -M_a^* \dot{V} + F_Z', \tag{50}$$

where

$$M_a^* = \int_0^{\ell} \rho n_Z \left[\overline{\mathbb{Q}}_{22}\right] \{n_Z\} H_1 \, dy_1, \quad F_Z' = \int_0^{\ell} (p_1+p_3) n_Z H_1 \, dy_1. \tag{51}$$

Substitution from Eq. (50) into Eq. (45a) gives

$$(M^* + M_a^*)\dot{V}(t) = F_Z' - M^* g. \tag{52}$$

Eq. (52) is numerically integrated by using the following algorithm:

$$(M^* + M_a^*)\dot{V}^{n+1} = F_Z'(t_{n+1}) - M^* g, \tag{53a}$$

$$V^{n+1} = V^n + \frac{1}{2}\left(\dot{V}^{n+1} + \dot{V}^n\right)\delta t, \tag{53b}$$

$$\xi^{n+1} = \xi^n + V^n \delta t + \frac{1}{2}\dot{V}^n \delta t^2, \tag{53c}$$

where

$$V^{n+1} = V(t_{n+1}), \quad \xi^{n+1} = \xi(t_{n+1}). \tag{54}$$

Here ξ is the submergence, shown in Fig. 1, of the panel apex with respect to the undisturbed water surface. The velocity and acceleration of the panel apex are assumed to be equal to the rigid body motion velocity and acceleration respectively since the edge at the apex is assumed not to deform. The acceleration of the rigid body motion can be evaluated from Eq. (52), and the rigid body displacement and velocity are updated by using, respectively, the forward and the central difference methods; e.g., see Eqs. (53b) and (53c).

Using Eq. (49a), we write the force vector in Eq. (44) as

$$\boldsymbol{F}^{ext} = \int_0^{\ell} \left[\Phi\left(y_1, -h^b - h^c\right)\right]^T \begin{Bmatrix} -F_{31} \\ F_{11} \end{Bmatrix} (p_1+p_2+p_3) H_1 \, dy_1 + \boldsymbol{F}^{rig} = -\mathbf{M}_a \ddot{\boldsymbol{d}} + \boldsymbol{F}^{pre} + \boldsymbol{F}^{rig}, \tag{55}$$

where we have substituted for p_1 from Eq. (49b), and

$$\boldsymbol{F}^{pre} = \int_0^{\ell} \left[\Phi\left(y_1, -h^b - h^c\right)\right]^T \begin{Bmatrix} -F_{31} \\ F_{11} \end{Bmatrix} (p_2+p_3) H_1 \, dy_1, \tag{56a}$$

$$\boldsymbol{M}_a = \int_0^{\ell} \left[\Phi\left(y_1, -h^b - h^c\right)\right]^T \begin{Bmatrix} -F_{31} \\ F_{11} \end{Bmatrix} \rho [\overline{\mathbb{Q}}_{22}] \, [\mathbb{C}] H_1 \, dy_1. \tag{56b}$$

Here $\boldsymbol{M}_a$ is called the added mass matrix due to vibrational motion of the panel and $\boldsymbol{F}^{pre}$ is the external force vector due to the hydrodynamic pressure without considering vibrational acceleration. We note that Qin and Batra (2009) used a semi-analytical approach for studying motion of the fluid and found an expression for the added mass matrix.

Thus equation of motion (44a) of the panel becomes

$$(\mathbf{M} + \mathbf{M}_a)\ddot{\boldsymbol{d}} + \boldsymbol{C}\dot{\boldsymbol{d}} + \boldsymbol{K}(\boldsymbol{d})\boldsymbol{d} = \boldsymbol{F}^{pre} + \boldsymbol{F}^{rig} + \boldsymbol{F}^c. \tag{57}$$

Eq. (57) is used to update the vibrational acceleration, velocity and deformations of the solid body. It is integrated by using the following conditionally stable central-difference method:

$$\boldsymbol{d}^{n+1} = \boldsymbol{d}^n + \delta t \dot{\boldsymbol{d}}^n + \frac{\delta t^2}{2}\ddot{\boldsymbol{d}}^n, \tag{58a}$$

$$\left(\boldsymbol{M} + \boldsymbol{M}_a + \frac{\delta t}{2}\boldsymbol{C}\right)\ddot{\boldsymbol{d}}^{n+1} = \boldsymbol{F}^{rig}(t_{n+1}) + \boldsymbol{F}^{pre}(t_{n+1}) + \boldsymbol{F}^c(t_{n+1}) - \boldsymbol{K}\left(\boldsymbol{d}^{n+1}\right)\boldsymbol{d}^{n+1} - \boldsymbol{C}\left(\dot{\boldsymbol{d}}^n + \frac{\delta t}{2}\ddot{\boldsymbol{d}}^n\right), \tag{58a}$$

$$\dot{\boldsymbol{d}}^{n+1} = \dot{\boldsymbol{d}}^n + \frac{\delta t}{2}\left(\ddot{\boldsymbol{d}}^{n+1} + \ddot{\boldsymbol{d}}^n\right), \tag{58c}$$

where

$$\boldsymbol{d}^{n+1} = \boldsymbol{d}(t_{n+1}). \tag{59}$$

The flow chart for iteratively solving the FSI problem is given in Fig. 5. Using the known solution at time t_n, $\ddot{\boldsymbol{d}}^{n+1}$, $\dot{\boldsymbol{d}}^{n+1}$, $\dot{\boldsymbol{V}}^{n+1}$ and $\boldsymbol{V}^{n+1}$ can be evaluated by using Eqs. (58) and (53). These quantities are used to update φ and Ψ for the next iteration. The iterative process is terminated when the normalized difference of computed total pressure between two successive iterations is less than the prescribed tolerance of 10^{-4}. The normalized difference of pressure between iterations $I+1$ and I is defined as $\int_0^{\ell} |p_4^{I+1} - p_4^I| ds / \int_0^{\ell} |p_4^{I+1}| ds$ where $p_4^I = p - p_a$ is the total pressure on the wedge at iteration I. The procedure discussed above to analyze the FSI problem is called the added mass method.

The critical time step size δt_s to compute a stable solution for the structure part is determined by finding the maximum frequency, ω_{max}, of free vibrations and taking $\delta t_s \le \delta t_{crit}$, $\Delta t_{crit} = 2/\omega_{max}$. Ideally, ω_{max} should be found after every time step since frequencies of a structure change as it is deformed. The accuracy of the solution can be improved by taking $\delta t_s \ll \delta t_{crit}$ but at the cost of increasing the computational time.

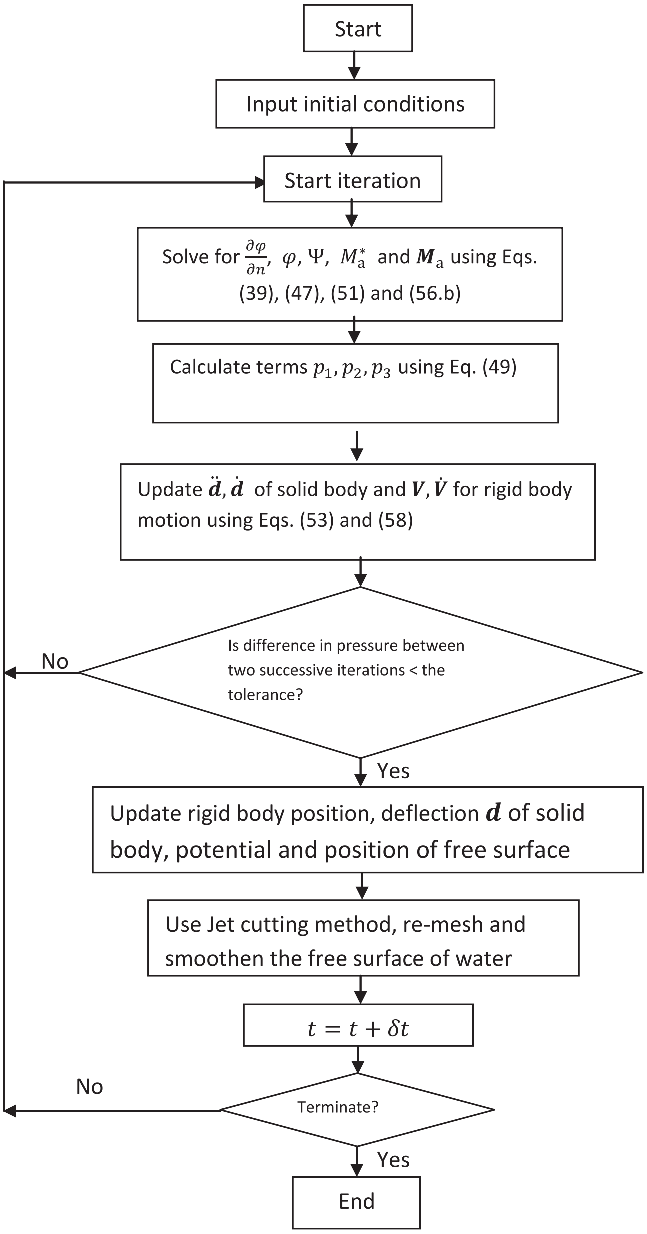

Fig. 5. Flow chart for the analysis of the FSI problem by the coupled BE–FE method.

Results presented in Section 4 have been computed with a consistent mass matrix and $\delta t_s = 0.9\delta t_{crit}$ for linear problems but $\delta t_s = 0.5\delta t_{crit}$ for nonlinear problems. For the nonlinear problems, ω_{max} found from analyzing frequencies of the undeformed beam is used to determine δt_{crit}. $\boldsymbol{M}_a$ is not considered when evaluating ω_{max}.

As mentioned by Xiao and Batra (2012) the time step δt_f for integrating, with respect to time, Eq. (3) for motion of the fluid is given by

$$\delta t_f = \frac{h_{min} 2 \tan \beta}{V \pi \gamma_t}, \tag{60}$$

where h_{min} is the minimum element length near the jet tip, γ_t is assigned values between 2 and 20, and we use $\gamma_t = 5$. For the water slamming of a curved panel shown in Fig. 14, we choose β as the minimum of the local deadrise angles at nodes on the panel/fluid interface, slope of the free water surface at nodes on it, and the local angle at the jet tip.

The time step δt for the FSI analysis equals the smaller of δt_f and δt_s.

3.4. Verification of the code

The verification of the FE software for analyzing deformations of the panel is described in Batra and Xiao (2013b) and the verification of the FE software for delamination analysis is discussed in Batra and Xiao (2013a). The developed BE software has been verified in Xiao and Batra (2012) by using the method of manufactured solutions (e.g., see the material just preceding and following Eq. (20) of Batra and Liang (1997)). The coupling between the two software is verified by analyzing problems for rigid panels and comparing computed results with those available in the literature, e.g., see Xiao and Batra (2012).

4. Example problems

We discretize the fluid domain boundary into two-node elements with nodes at the end points of the element, and with node numbers starting from point $\mathcal{C}$ in Fig. 6 and going counter-clockwise ($\mathcal{CDEABC}$), and denote the length of element j with nodes j and $j+1$ by h_j. Non-uniform meshes are used to discretize the free surface of water near the jet tip $\mathcal{A}$, the fluid boundary $\mathcal{AB}$ on the panel and the fluid boundary $\mathcal{BC}$ on the axis of symmetry. In Fig. 6 the free surface of water near the panel edge is exhibited in which points $\mathcal{A}$ and $\mathcal{B}$ are, respectively, points of intersection between the free surface and the panel, and the panel and the axis of symmetry. The length, h_j, of element j on the free surface boundary $\mathcal{EA}$ for mesh 1 is chosen according to the following empirical criteria:

$$h_j = \begin{cases} d_{34}, & \overline{N}_{\mathcal{A}} - 100 \le j < \overline{N}_{\mathcal{A}}, \\ \min\left(d_{33},\ 1.05^{\overline{N}_{\mathcal{A}} - 100 - j} d_{34}\right), & j < \overline{N}_{\mathcal{A}} - 100 \text{ and } \zeta_{\mathcal{A}j} \le 1.0\mathscr{L}, \\ d_{32}, & 1.0\mathscr{L} < \zeta_{\mathcal{A}j} \le 2.0\mathscr{L} \\ d_{31}, & \zeta_{\mathcal{A}j} > 2.0\mathscr{L} \end{cases} \tag{61}$$

$d_{31} = L_1/40$, $d_{32} = 1/75$, $d_{33} = d_{32}/5$, $d_{34} = d_{32}/b_r$.

Here b_r is the mesh refinement parameter whose value depends upon the deadrise angle, $\mathscr{L}$ equals the arc length of the panel, $\zeta_{\mathcal{A}j}$is the arc length between points $\mathcal{A}$ and j, and $\overline{N}_{\mathcal{A}}$ is the node number of point $\mathcal{A}$.

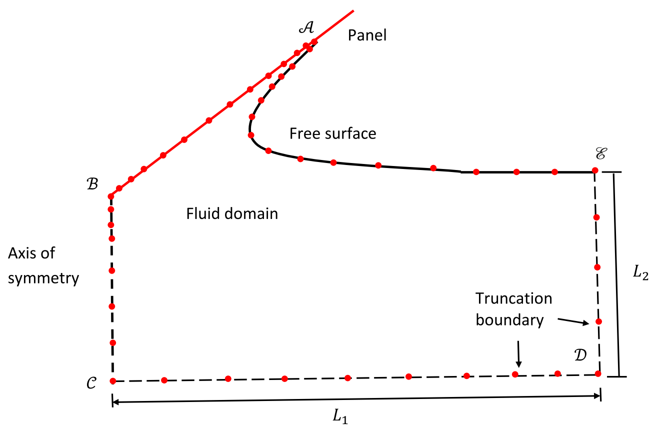

Fig. 6. Discretization of the boundary of the fluid domain into elements.

Table 1
Values of material parameters of the sandwich panel.

	C_{1111} (GPa)	C_{1133} (GPa)	C_{3333} (GPa)	C_{1313} (GPa)	Mass density (kg/m^3)
Face sheet	140.3	3.77	9.62	7.10	31,400
Core	3.77	1.62	3.77	1.08	150

A non-uniform mesh with element size h_j given by Eq. (61) is used to discretize the water surface $\mathcal{AB}$ contacting the panel with smaller elements near points $\mathcal{A}$ and $\mathcal{B}$ than those elsewhere.

$$h_j = \begin{cases} d_{34}, & \overline{N}_{\mathcal{A}} \le j \le \overline{N}_{\mathcal{A}} + 100, \\ \min\left(d_{32},\ 1.05^{j-(\overline{N}_{\mathcal{A}}+100)} d_{34}\right), & j > \overline{N}_{\mathcal{A}} + 100 \text{ and } \zeta_{\mathcal{A}j} \le \zeta_{\mathcal{AB}} - 0.1\mathcal{L}, \\ 0.5 d_{32}\ , & j > \overline{N}_{\mathcal{A}} + 100 \text{ and } \zeta_{\mathcal{A}j} > \zeta_{\mathcal{AB}} - 0.1\mathcal{L}. \end{cases} \tag{62}$$

This scheme generates finer meshes near points $\mathcal{A}$ and $\mathcal{B}$. The length h_j of element j on the axis of symmetry $\mathcal{BC}$ is taken to be given by

$$h_j = \min(d_{31},\ 1.2^{j-\overline{N}_{\mathcal{B}}} h_{\overline{N}_{\mathcal{B}}-1}). \tag{63}$$

Here $\overline{N}_{\mathcal{B}}$ is the node number of point $\mathcal{B}$. The element length on the truncation boundaries $\mathcal{CD}$ and $\mathcal{DE}$ equals d_{31}. Lengths of elements for mesh 2 are the same as those for mesh 1 except that $d_{31} = L_1/80$ and $d_{32} = 1/150$. Thus the element length for mesh 2 is one-half of that for mesh 1 in most of the region on the boundary. Unless otherwise specified, results presented below have been computed with mesh 2 and $b_r = 20$.

4.1. Water slamming of linear elastic straight sandwich panel

We now analyze deformations of a clamped–clamped linear elastic straight sandwich panel of length $\mathcal{L} = 1$ m, thickness of each face sheet $h^b = h^t = 1.2$ cm, core thickness $2h^c = 3.0$ cm, and downward impact velocity = 10 m/s. Effects of gravity have been neglected. Values of material parameters are listed in Table 1. The mass density assigned to face sheets includes the dead weight of the ship. The sandwich panel is divided into 60 uniform 2-node elements along the y_1-axis, the fluid domain is discretized using mesh 2 with b_r=40, and L_1 and L_2 are set equal to 15 m. As shown through numerical experiments in Das and Batra (2011) these values of b_r, L_1 and L_2 give converged results. The time steps used to compute results found by using the criterion discussed in Section 3.3 equaled 0.19 μs, 0.37 μs, 0.53 μs for deadrise angle, β=5°, 10°, and 14°, respectively.

The hydroelastic effects are influenced by the stiffness of the structure, deadrise angle of the panel and the downward velocity. Stenius et al. (2011) have proposed that for panels modeled as Euler–Bernoulli beams the hydroelastic effects can be characterized by the factor $\overline{R}$ defined as

$$\overline{R} = 4\left(\frac{\mu_{NP}}{\pi}\right)^2 \frac{\tan\beta}{V} \sqrt{\frac{D}{\pi\rho L^3}}, \tag{64}$$

where

$$D = \frac{1}{3}\left[E^t\left(\left(h^c + h^b\right)^3 - \left(h^c\right)^3\right) + 2E^c\left(h^c\right)^3 + E^b\left(\left(h^c + h^b\right)^3 - \left(h^c\right)^3\right)\right]. \tag{65}$$

Here μ_{NP} is a boundary condition parameter ($\mu_{NP} = 4.73$ for clamped–clamped edges), D is effective bending stiffness of the sandwich panel based on the Euler Bernoulli beam theory, E^t, E^c and E^b are Young's moduli in the axial-direction for the top, the core and the bottom layers, respectively, of the sandwich beam. In Stenius et al. (2011) hydroelastic deformations of a homogeneous material beam were studied, D and $\overline{R}$ equaled, respectively, the bending stiffness of the panel and the ratio of twice the loading period to the fundamental frequency of the panel modeled as Euler–Bernoulli beam. The appropriateness of using R for a sandwich beam requires detailed analyses of different combinations of materials and thicknesses for the core and the face sheets, as well as computing results for rigid panels. This exercise is left for a future study. It is shown in Stenius et al. (2011) that for $\overline{R} > 4$ hydroelastic effects are negligible in the sense that the pressure determined from the assumption of the panel being rigid will result in the same deflection profile of the panel as that from the analysis of the coupled hydroelastic problem. For the sandwich panel, other factors such as delamination between face sheets and the core will influence deflections of the panel. For the problem being studied, $\overline{R}$ equals 1.7, 3.5 and 4.9 for β=5°, 10°, and 14°, respectively.

For the panel of initial deadrise angle β=5° we set the Rayleigh damping coefficient $\alpha = 5 \times 10^{-6}$. As should be clear from the time history of the pressure at y_1=0.35 m plotted in Fig. 7, oscillations in the pressure have been significantly diminished, and the difference in results computed with $\alpha = 5 \times 10^{-6}$ and 5×10^{-7} is miniscule. The pressure computed without using the added mass method exhibits oscillations at t=4 ms whereas that with the added mass method does not. Results presented below have been computed with the added mass method.

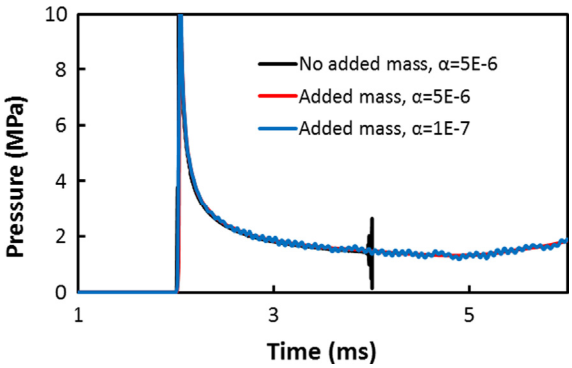

Fig. 7. For initial downward impact speed = 10 m/s and deadrise angle = 5°, time histories of the pressure on the panel at $y_1 = 0.35$ m for two values of the damping ratio, and with and without adding mass due to acceleration of particles on the panel surface. The three curves overlap each other.

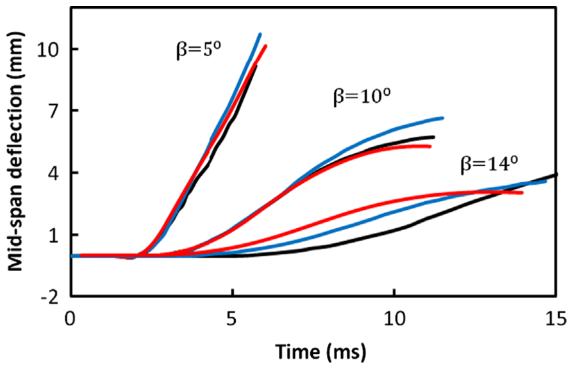

Fig. 8. For initial impact speed = 10 m/s, time histories of the panel centroid deflection for initial deadrise angle = 5°, 10° and 14°. Black, blue and red curves represent, respectively, results from Qin and Batra (2009), Das and Batra (2011), and the present work. (For interpretation of the references to color in this figure legend, the reader is referred to the web version of this article.)

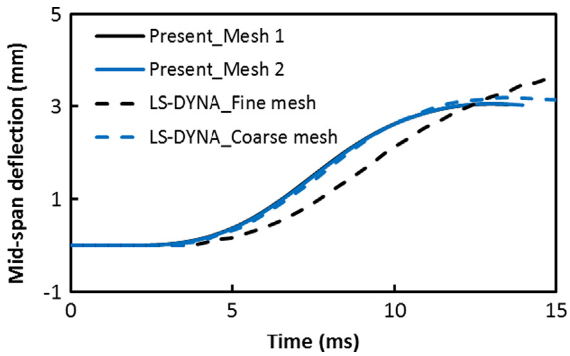

Fig. 9. For initial deadrise angle = 14° and initial impact speed = 10 m/s, time histories of the deflection of the centroid of the panel found by using different meshes. Results from FE meshes 1 and 2 are indistinguishable from each other in the plots. Curves marked LSDYNA denote results from Das and Batra (2011).

In Fig. 8 the presently computed time histories of the deflection of the panel centroid for three different values of the initial deadrise angle are compared with those found by Das and Batra (2011) who used LSDYNA and by Qin and Batra (2009) who employed a semi-analytical approach. Solutions from the three methods are close to each other for initial deadrise angles of 5° and 10°, but differences among them are large for initial deadrise angle of 14°. Results obtained by using the three meshes for the panel of initial deadrise angle 14° plotted in Fig. 9 suggest that they are essentially unchanged and are closer to the results from the coarse rather than the fine mesh employed by Das and Batra (2011). We note that Qin and Batra (2009) used simplifications valid for small values of the initial deadrise angle of the panel. The deformed shapes at $t = 5.47$ ms of the mid-surface of the panel of initial deadrise angle = 5° computed by the three methods plotted in Fig. 10 are close to each other, with percentage difference, $100 \int_0^{\mathscr{L}} |u_3 - u_3^{pre}| ds / \int_0^{\mathscr{L}} |u_3^{pre}| ds$, equal to 10% and 6.2%,

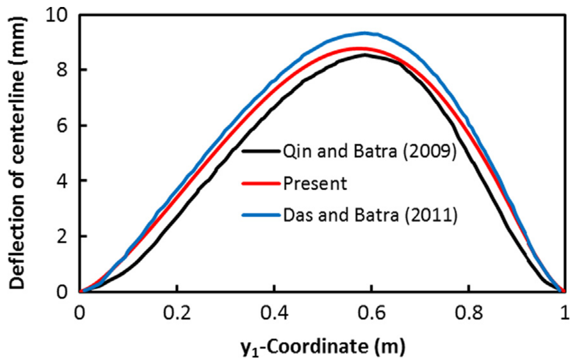

Fig. 10. At $t=5.471$ ms after impact, deformed shapes of the mid-surface of the panel computed by the three methods.

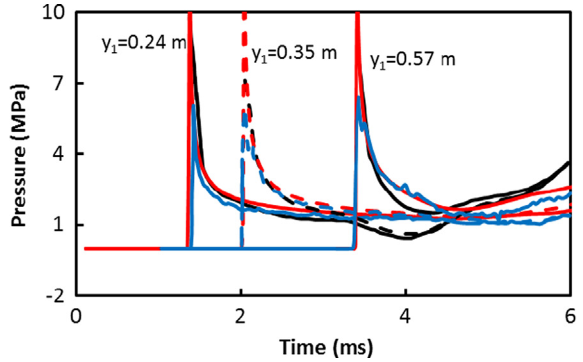

Fig. 11. Time histories of the pressure at three locations of the panel of initial deadrise angle 5°. Black, blue and red curves represent, respectively, results from Qin and Batra (2009), Das and Batra (2011), and the present method. (For interpretation of the references to color in this figure legend, the reader is referred to the web version of this article.)

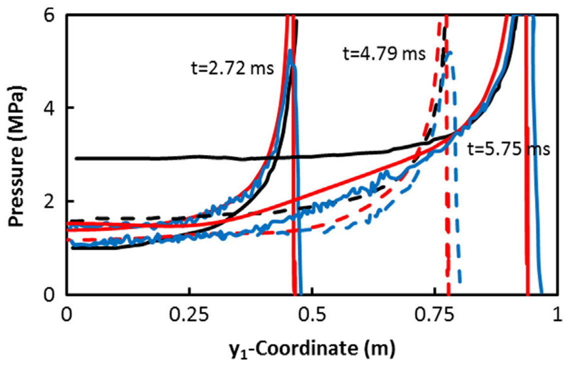

Fig. 12. Pressure distribution on the panel of initial deadrise angle=5° at $t=2.72$, 4.79 and 5.75 ms. Black, blue and red curves represent results computed, respectively, by Qin and Batra (2009), Das and Batra (2011), and the present method. (For interpretation of the references to color in this figure legend, the reader is referred to the web version of this article.)

respectively, for solutions of u_3 given in Qin and Batra (2009) and Das and Batra (2011). Here, u_3^{pre} is the presently computed value of u_3.

Fig. 11 exhibits time histories of the slamming pressure at locations $y_1=0.24$, 0.35 and 0.57 m of the panel of initial deadrise angle=5°, and Fig. 12 shows the pressure variations on the panel at time $t=2.72$, 4.79 and 5.75 ms. The peak pressure predicted by the present method is very high and qualitatively resembles that given by Qin and Batra's (2009) semi-analytical approach, and it is much higher than that found by Das and Batra (2011) using LSDYNA. We note that in the

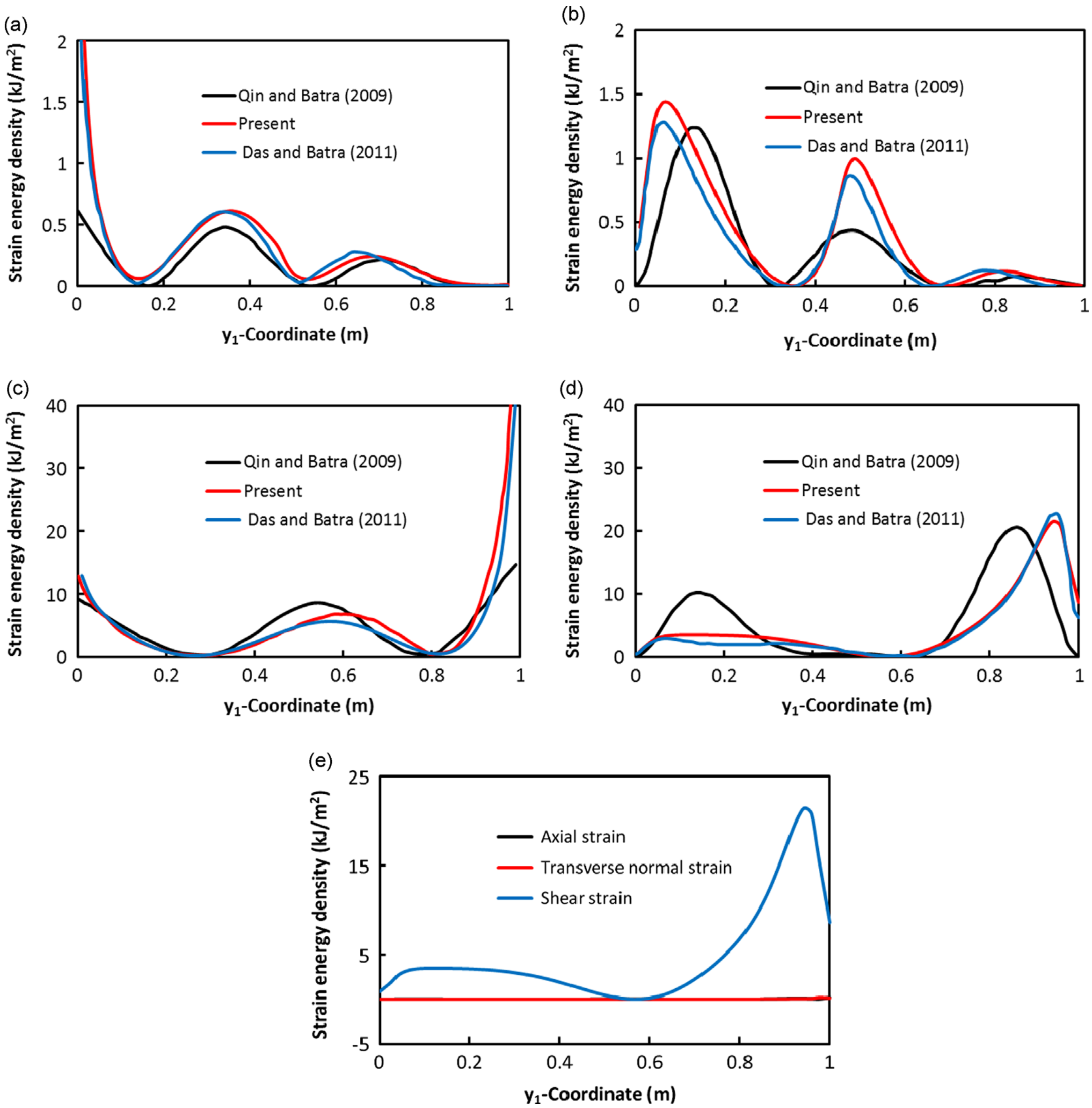

Fig. 13. Variation of the strain energy density in the face sheets and the core along the panel span when $t = 2.74$ ms and 6.02 ms (initial deadrise angle = 5°). (a) At t = 2.74 ms, the spatial variation of the strain energy density in the face sheets, (b) At t = 2.74 ms, the spatial variation of the strain energy density due to the transverse shear strain in the core, (c) At t = 6.02 ms, the variation of total strain energy density in the two face sheets along the panel span, (d) At t = 6.02 ms, the variation along the panel span of the strain energy density in the core due to the transverse shear strain, and (e) At t = 6.02 ms, variation along the panel span of the strain energy density in the core due to different strain components. The curve for the axial strain coincides with that for the transverse shear strain.

Table 2
Comparison of LSDYNA and coupled BE–FE approaches for the water slamming problem.

	LSDYNA	BE–FE methods
Fluid penetrates into solid	Yes	No
Oscillations in pressure on the panel	Yes	No
Results depend on contact algorithm	Yes	No
Computation of water jet	Difficult	Easy
Assumptions for fluid motions	Compressible	Incompressible and irrotational
Evaluation of motion at a point in the fluid domain	Easy	Difficult

modified Wagner's theory employed in Qin and Batra (2009) the pressure field is singular and its peak value is approximated. Except for the peak pressure, the three methods give results that are close to each other.

The strain energy density is computed by using Eq. (18). Contributions to the strain energy density due to the transverse shear strain, the axial strain and the transverse normal strain equal, respectively, $C_{1313}E_{13}{}^2$, $\frac{1}{2}C_{1111}E_{11}^2$ and $\frac{1}{2}C_{3333}E_{33}^2$. Taking

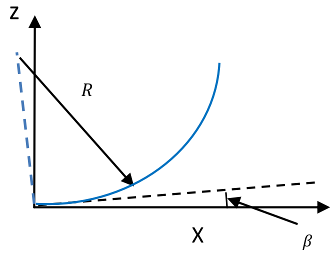

Fig. 14. Sketch of the undeformed circular panel, and of the local deadrise angle at the point of impact.

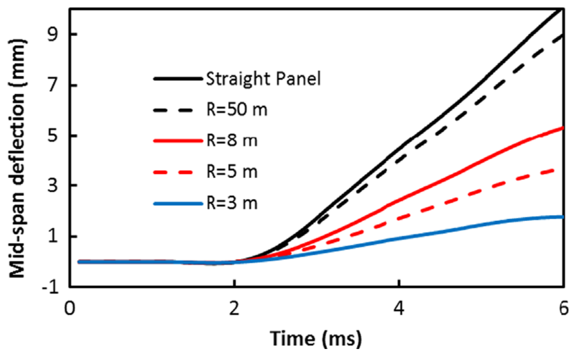

Fig. 15. Time histories of the deflection of the mid-span of the panel.

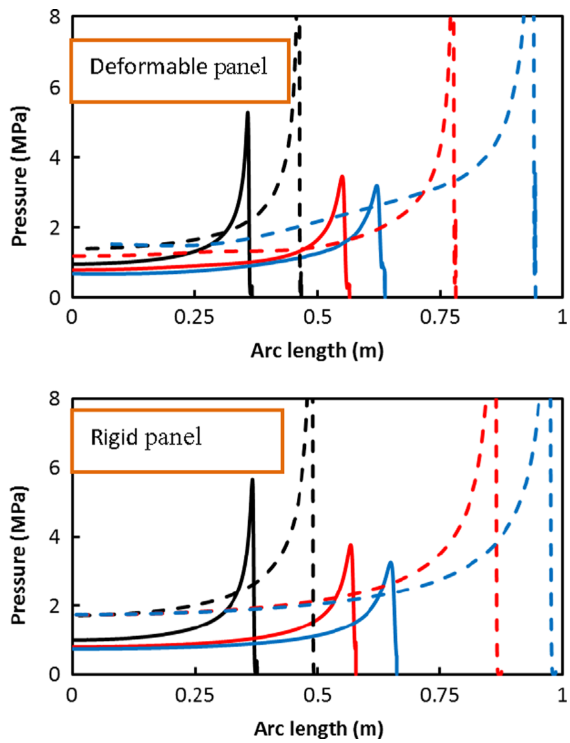

Fig. 16. Pressure distribution on the deformable and rigid panels at different times. Solid (dashed) curves represent pressure distribution on the circular (straight) panel of $R=5$ m (infinity). Black, red and blue curves represent results at $t=2.72$, 4.79 and 5.75 ms, respectively. (For interpretation of the references to color in this figure legend, the reader is referred to the web version of this article.)

the panel dimension in the y_2-direction as 1 m, strain energy densities stored in the core and the two face sheets at $t=2.74$ ms and 6.02 ms are plotted in Fig. 13 along with those from Das and Batra (2011). The core of the sandwich panel absorbs significant amount of energy due to transverse shear deformations which agrees with that reported by Qin and Batra (2009) and Das and Batra (2011). Deformations of the panel were assumed to be infinitesimal in Qin and Batra (2009) but all geometric nonlinearities were considered in Das and Batra (2011). We have listed in Table 2 salient features of solutions of the water entry problem using the FE software LSDYNA and the present coupled BE–FE approach.

4.2. Water entry of linear elastic circular sandwich panel

Sun and Faltinsen (2006) have considered hydroelastic effects in analyzing deformations of circular shells made of steel and aluminum. They studied motion of the fluid by the BEM and deformations of shells by the modal analysis. Here we analyze transient plane strain deformations of a circular sandwich panel with the mid-surface radius equal to R, deadrise angle $\beta=5°$at the initial point of impact (e.g., see Fig. 14), both edges rigidly clamped, and values of material parameters the same as those of the straight sandwich panel studied above. The length $\mathscr{L}$ equals the arc length of the curved beam.

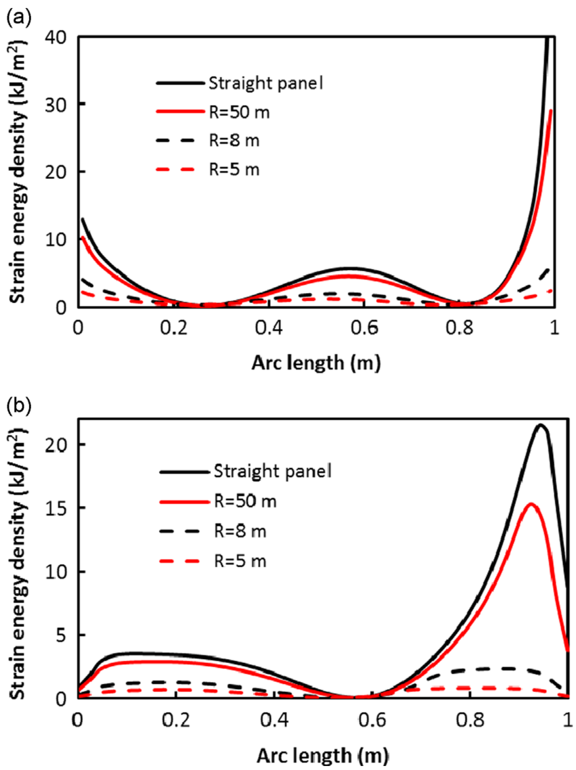

Fig. 17. For different radii of the circular panel and $t=6.02$ ms, variation along the panel span of: (a) the total strain energy density in the face sheets, and (b) the strain energy density due to transverse shear strain in the core.

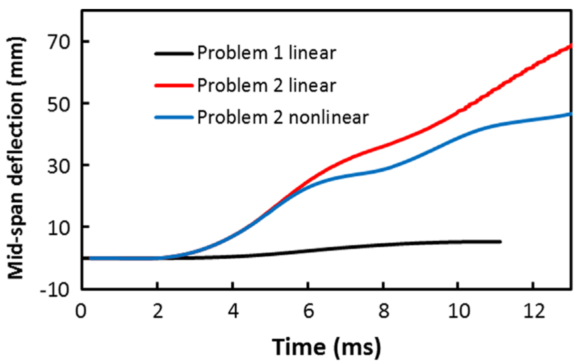

Fig. 18. Time histories of the panel centroid deflection.

From time histories of the panel centroid deflection for different values of R displayed in Fig. 15, it is transparent that with an increase in the value of R, the centroidal deflection approaches that of a straight panel as it should. Also, at a fixed time, the deflection increases with an increase in R which could be due to the dependence upon R of the wetted length and

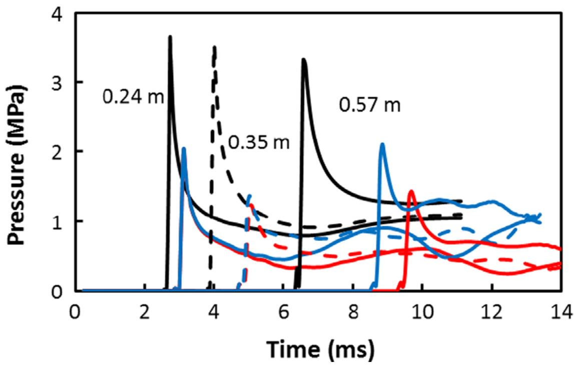

Fig. 19. Time histories of the hydroelastic pressure on the panel at three points with arc length in the deformed shape equal to 0.24 m, 0.35 m and 0.57 m. Black, red and blue curves represent results for linear problem 1, linear problem 2 and nonlinear problem 2, respectively. (For interpretation of the references to color in this figure legend, the reader is referred to the web version of this article.)

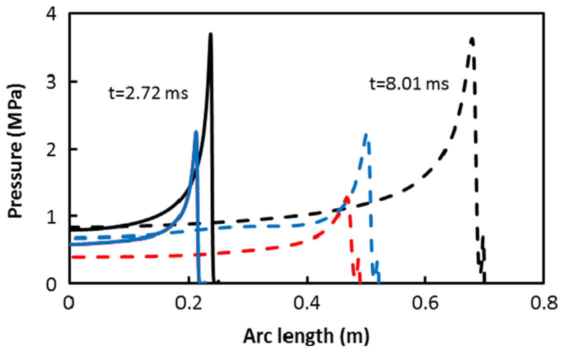

Fig. 20. Distribution of the hydroelastic pressure on the panel at $t=2.72$ and 8.01 ms. Black, red and blue curves represent results for linear problem 1, linear problem 2, and nonlinear problem 2, respectively. At $t=2.72$ ms, the red curve overlaps the blue curve as the geometric nonlinear effect is insignificant when deformations are infinitesimal. (For interpretation of the references to color in this figure legend, the reader is referred to the web version of this article.)

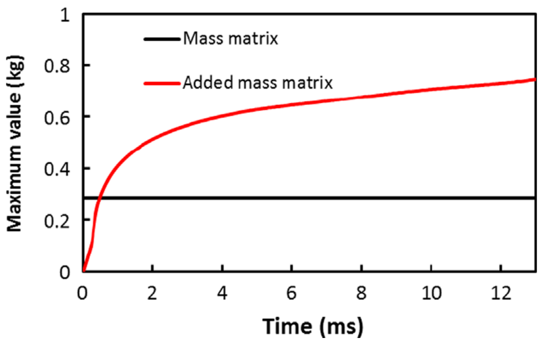

Fig. 21. Time histories of the maximum value of an element of the mass matrix $\boldsymbol{M}$ and of the added mass matrix $\boldsymbol{M}_a$ for linear problem 2.

Table 3
Values of material parameters of the sandwich panel.

	C_{1111} (GPa)	C_{1133} (GPa)	C_{3333} (GPa)	C_{1313} (GPa)	Mass density (kg/m^3)
Face sheet	13.4	2.40	5.92	1.92	1850
Core	0.307	1.62	0.0923	0.107	200

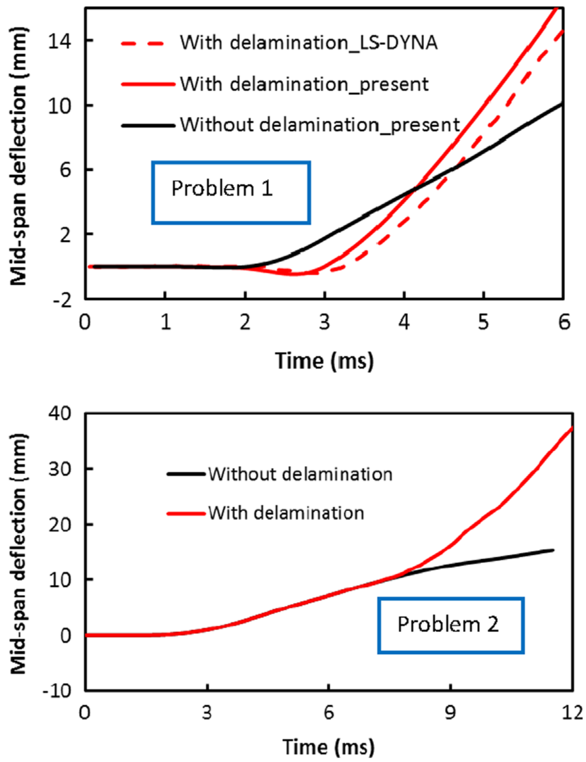

Fig. 22. Time histories of the deflection of the straight panel centroid with and without considering delamination.

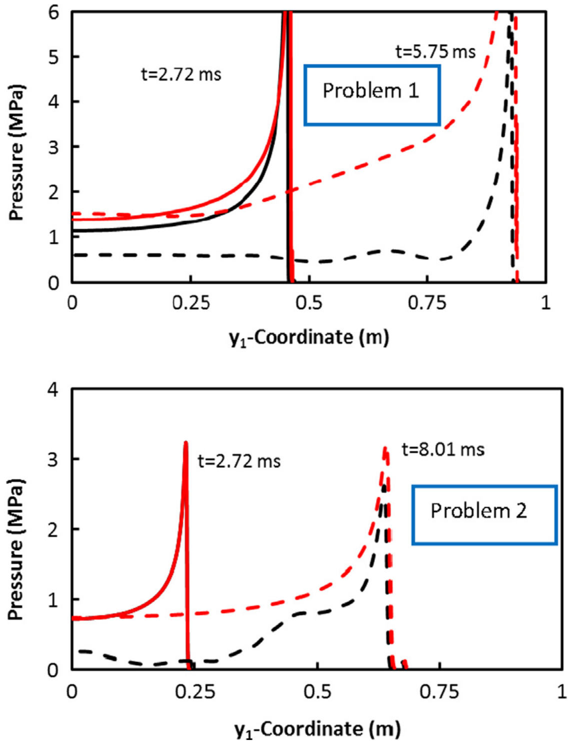

Fig. 23. Distribution of the hydroelastic pressure on the panel at two different times. Black and red curves represent results with and without considering delamination, respectively. The red and black curves at $t = 2.72$ ms for problem 2 overlap as the beam has not been delaminated at this time. (For interpretation of the references to color in this figure legend, the reader is referred to the web version of this article.)

of the pressure distribution. We have exhibited in Fig. 16 the variation of the hydroelastic pressure on curved and straight panels at $t=2.72$, 4.79 and 5.75 ms. It is clear that the curvature of the panel noticeably affects the magnitude of the peak pressure and the pressure distribution on the panel. The peak pressure on the circular panel is considerably less than that on the flat panel. As deformations of the panel are infinitesimal the maximum difference in the hydrodynamic pressure on rigid and deformable panels is small. Both for circular and flat panels, the pressure distribution on the panel can be viewed as a traveling wave with the peak pressure acting at the just wetted point, the pressure rapidly decreasing in its wake, and staying uniform over a significant part of the wetted length. We note that Henke (1994) studied deformations of a plate under a traveling load to simulate deformations induced by water slamming loads.

At $t=6.02$ ms and four values of R, variations of the strain energy density in the core and the face sheets along the panel span plotted in Fig. 17 reveal that at a point on the panel the strain energy densities in the core and the face-sheets decrease with a decrease in the value of R. When the entire panel has been wetted, the strain energy densities due to the transverse shear stain in the core and the total strain energy in the face sheets at points near the right edge are significantly larger than those at points near the left edge of the panel possibly due to the peak pressure acting near the right edge. Values of the strain energy densities at a point decrease with a decrease in the value of R.

4.3. Water entry of straight sandwich panel made of St. Venant–Kirchhoff material

Two water entry problems have been simulated to delineate the influence on the hydrodynamic pressure acting on a sandwich panel of geometric nonlinearities and panel stiffness. For problem 1 values of elastic constants are the same as those for the panel studied in Section 4.1, and for problem 2, values of all elastic parameters have been reduced by a factor of 10 and the mass density reduced to 2000 kg/m^3. For problem 2 we set $h^t=h^b=6$ mm, $h^c=7.5$ mm, and $\mathscr{L}=1$ m. The fundamental frequency for the beam of problems 1 and 2 without considering added mass and deformations of the beam are 110 and 101 Hz, respectively. The deadrise angle and the downward velocity of the panel for both problems

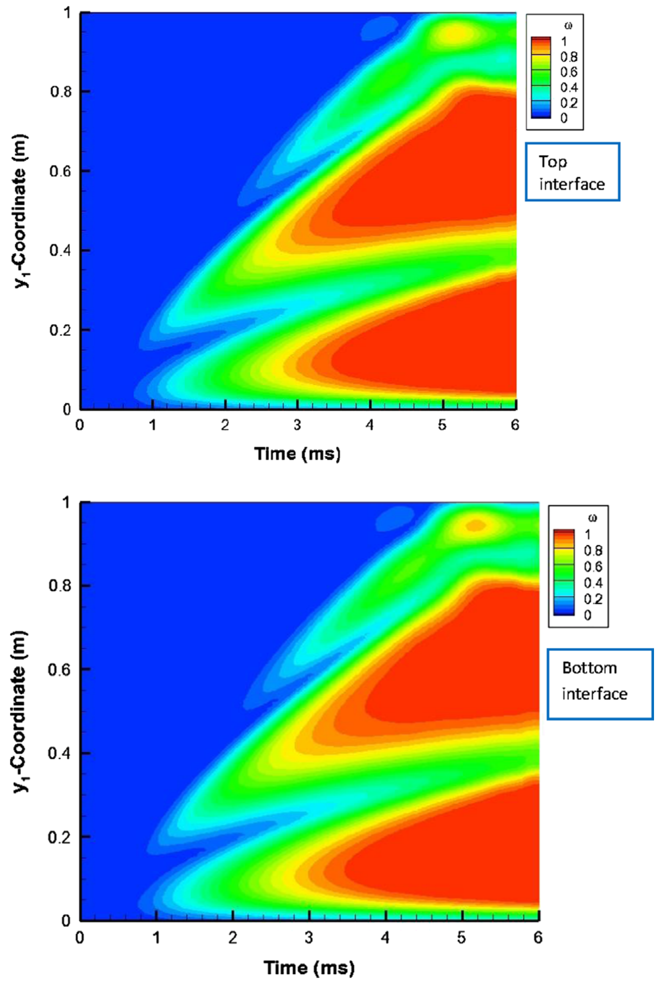

Fig. 24. Variation of the separation index ω with y_1-coordinate and time, on the top and the bottom interfaces for problem 1.

equal 10° and 10 m/s, respectively. The BE mesh 2 described at the beginning of Section 4 with the mesh refinement number $b_r = 20$ have been used. Effects of geometric nonlinearities are considered only for problem 2. The time step used to compute results equaled 0.75 μs for both problems. The hydroelastic factor $\overline{R}$ equals 3.5 and 0.39 for problems 1 and 2, respectively.

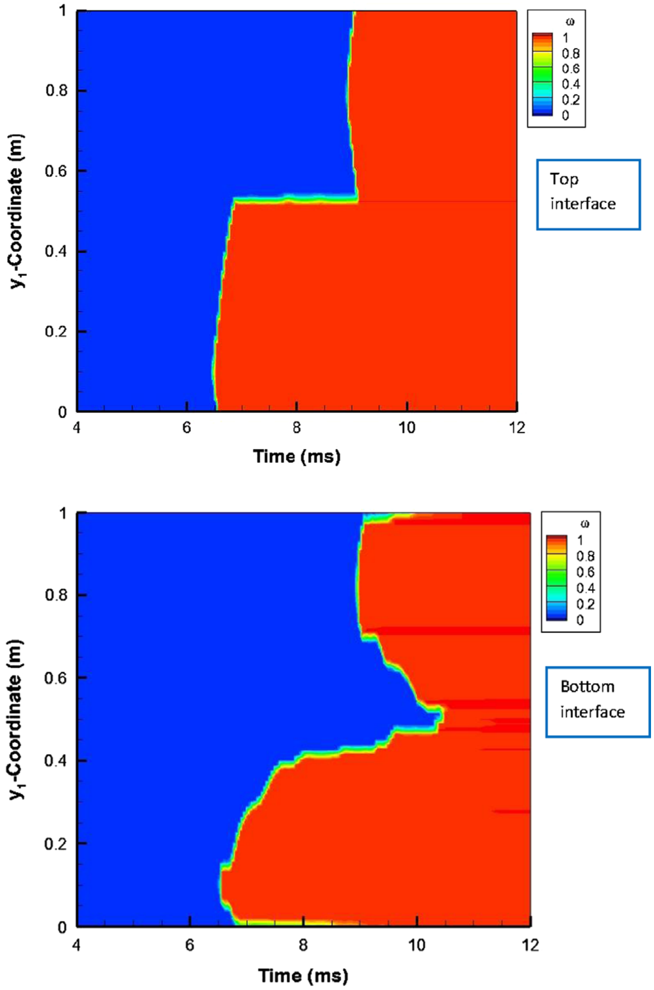

Fig. 25. Variation of the separation index ω with y_1-coordinate and time, on the top and the bottom interfaces for problem 2.

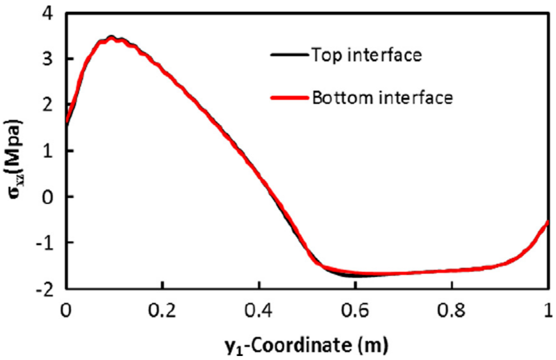

Fig. 26. Distribution of the transverse shear stress σ_{xz} on the top and the bottom interfaces at $t = 6.3$ ms for problem 2.

Time histories of the panel centroid deflection are plotted in Fig. 18. For problem 2, the maximum percentage difference $100|w_{lin} - w_{non}|/w_{lin}$ between the panel centroid deflections with (w_{non}) and without (w_{lin}) considering geometric nonlinearities is 32.5%. The time histories of centroidal deflections for the two linear problems suggest that the panel of problem 1 is considerably stiffer than that of problem 2 even though their fundamental frequencies are only 9% different. Recall that the fundamental frequency also depends upon the mass density, the panel thickness and the elastic moduli. From results for the two linear problems we deduce that the peak pressure on the stiffer panel that deflects less is nearly 80% more than that on the flexible panel. At a fixed value of time the wetted length is larger for the stiffer panel than that for the flexible panel.

Fig. 19 exhibits time histories of the hydrodynamic pressure on the panel at three different locations with arc length in the deformed shape equal to 0.24, 0.35, 0.57 m and Fig. 20 shows the pressure variations on the panel at times $t=2.72$ and 8.01 ms. These results suggest that the consideration of geometric nonlinearities significantly increases the maximum hydroelastic pressure acting on the panel. For example, at $x=0.57$ m, the peak hydroelastic pressures at $t \cong 9$ ms for the nonlinear problem equals 1.4 times that for the linear problem. It could be due to the fact that the stiffness of the panel considering geometrically nonlinear deformations is more than that of the identical panel for which geometric nonlinearities are not considered. At $x=0.57$ m, the peak hydroelastic pressure occurs sooner for the nonlinear problem than that for the linear problem. The traveling wave like behavior of the hydroelastic pressure is unaffected by the consideration of geometric nonlinearities.

Time histories of the maximum value of an element of the mass matrix $\boldsymbol{M}$ and the added mass matrix $\boldsymbol{M}_a$ for problem 2 considering infinitesimal deformations are exhibited in Fig. 21. It is clear that the added mass matrix increases significantly with an increase in the area of the contact surface between the panel and water. We note that the added mass matrix is due to the vibrational motion of the panel since its rigid body acceleration is null.

4.4. Delamination in linear elastic straight sandwich panel due to water slamming loads

We now analyze two problems involving delamination initiation and growth in a clamped–clamped linear elastic straight sandwich panel of length $\mathscr{L}=1$ m. The panel is divided into 81 uniform 2-node elements along the y_1-axis. The

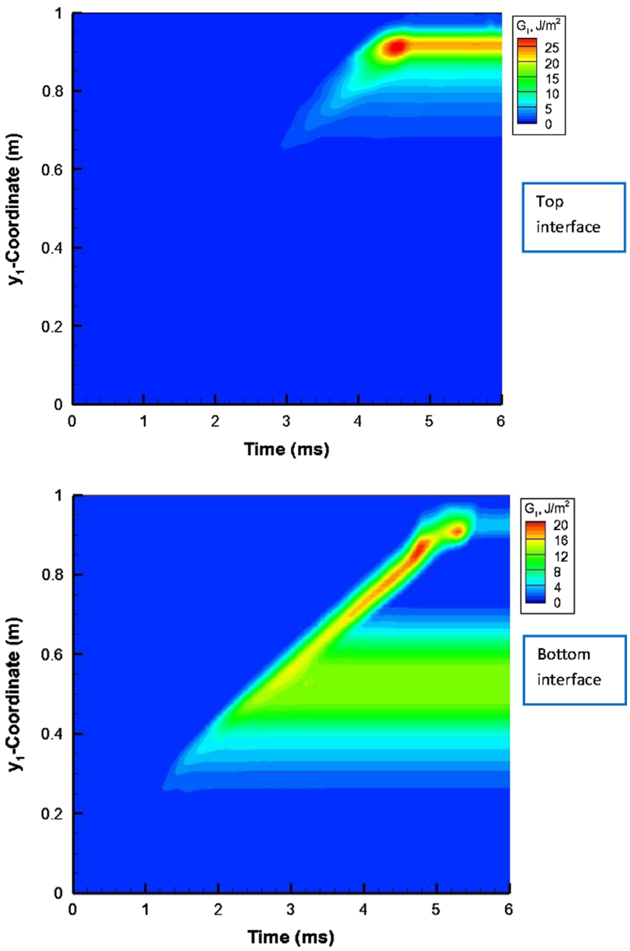

Fig. 27. Variation of the SERR G_I with y_1-coordinate and time, on the top and the bottom interfaces for problem 1.

fluid domain is discretized using mesh 2 described at the beginning of Section 4 with the mesh refinement number $b_r=40$ and 20, respectively, for problems 1 and 2. For problem 1, the geometric and material parameters, and the entry velocity are the same as those for the panel studied in Section 4.1 and the deadrise angle $\beta=5°$. We assume that the interface strength parameters have values $\sigma_t^0=\sigma_n^0=1$ MPa, $G_{Ic}=625\ \mathrm{J\,m^{-2}}$, $G_{IIc}=418\ \mathrm{J\,m^{-2}}$. Delamination in the panel of problem 1 has been studied by Das and Batra (2011) using LSDYNA and the above listed values of parameters. For problem 2, we assume that the thickness of each face sheet, $h^b=h^t=2$ cm, core thickness, $2h^c=6.0$ cm, downward impact velocity $=10$ m/s and deadrise angle $\beta=10°$. The face sheets and the core are assumed to be made of GRP and PVC foam (H200), respectively, and the interface parameters have values, $\sigma_t^0=3.5$ MPa, $\sigma_n^0=7.1$ MPa, $G_{Ic}=625\ \mathrm{J\,m^{-2}}$, $G_{IIc}=418\ \mathrm{J\,m^{-2}}$. The material properties for the face sheets and the experimental value of the critical interface SERR for mode II delamination are taken from Zenkert (1991). Values of the critical interface SERR for mode I delamination and the mass density of the GRP are not provided by Zenkert (1991), and these have been taken from Berggreen et al. (2007) and ⟨http://www.amiantit.com/media/pdf/brochures/Glass_Fibre_Reinforced_Products/files/Glass_Fibre_Reinforced_Products.pdf⟩, respectively. Values of material parameters for the core and the interface strength are taken from DIAB (2000). These values are listed in Table 3. The time steps used to compute results for problems 1 and 2 equaled 0.19 μs and 0.75 μs, respectively.

For problem 1, we compare the presently computed results with those of Das and Batra (2011) obtained by using LSDYNA and the stress criterion given by Eq. (27) to predict the delamination and failure of the interface. When using the stress criterion the failure occurs instantaneously when the criterion is satisfied. Fig. 22 exhibits time histories of the deflection of the panel centroid with and without considering delamination. It is clear that the presently computed results are close to those of Das and Batra (2011), and the panel centroid deflection considering delamination is larger than that without accounting for delamination. The stiffness of the sandwich panel decreases subsequent to the onset of delamination.

The variations of the hydroelastic pressure on the panel surface for two values of time are shown in Fig. 23. Consistent with the results presented in Figs. 16 and 19 the hydroelastic pressure on a delaminated panel is less than that on the corresponding in-tact panel because the panel stiffness is reduced due to delamination.

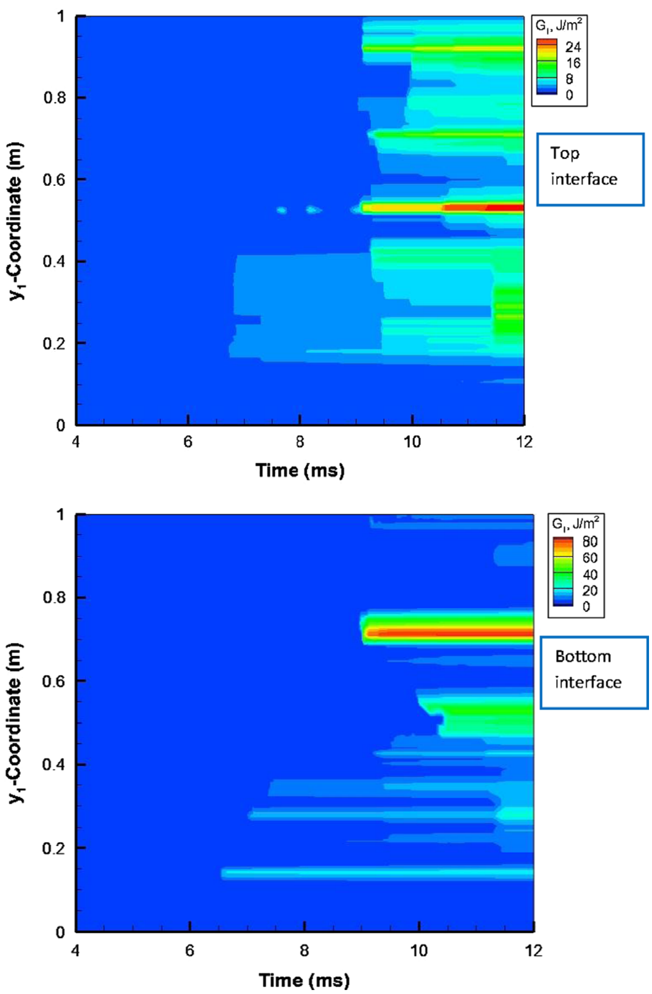

Fig. 28. Variation of the SERR G_I with y_1-coordinate and time, on the top and the bottom interfaces for problem 2.

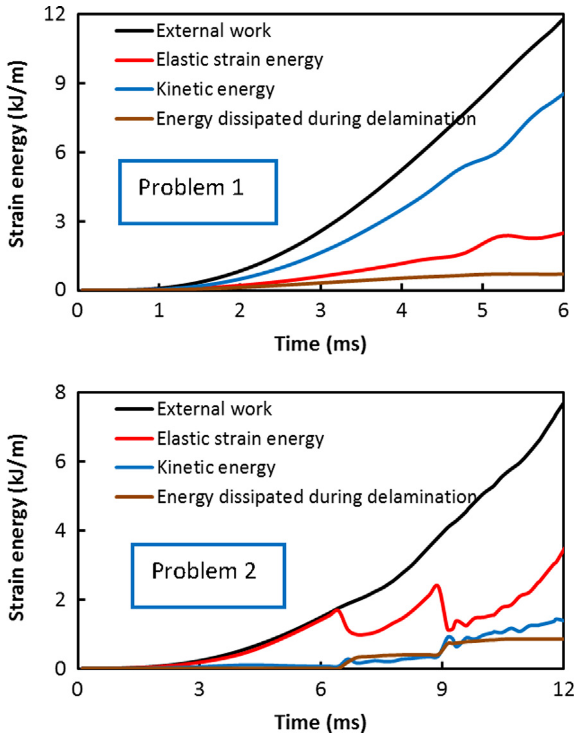

Fig. 29. Time histories of the work done by external forces, strain energy stored in the panel, kinetic energy and energy dissipated during delamination.

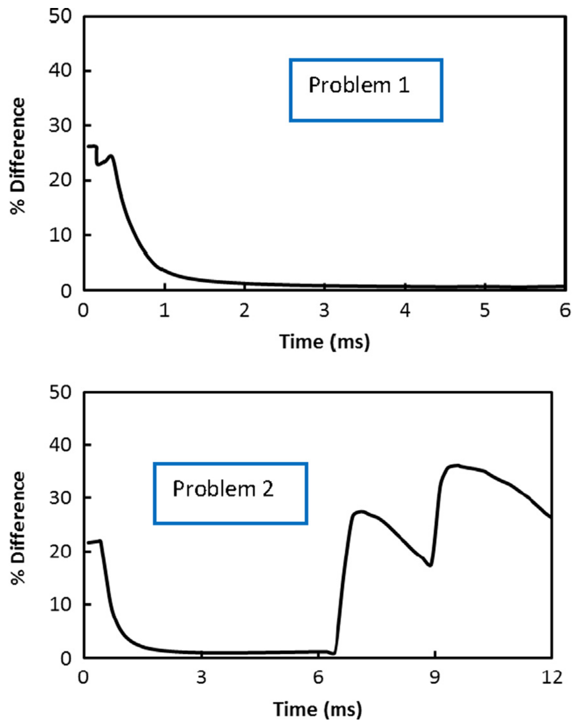

Fig. 30. Time history of the percentage difference, $100(W_p - W_e - W_d - W_k)/W_p$.

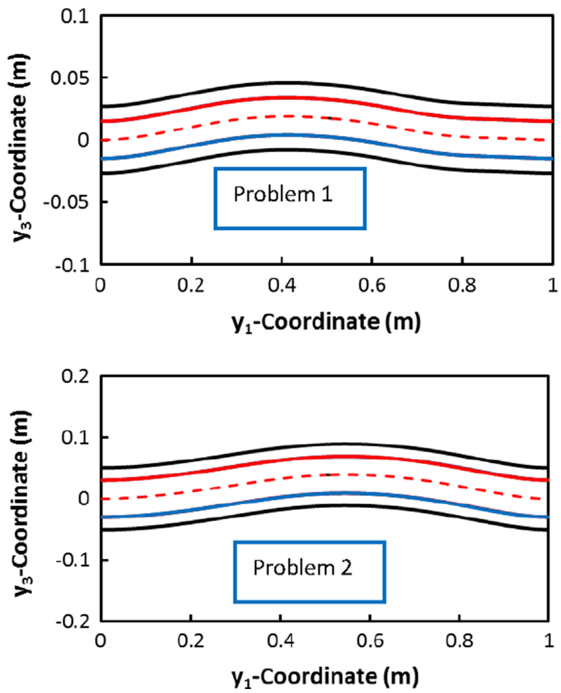

Fig. 31. Deformed shape of the sandwich panel when $t=6$ and 12 ms, respectively, for problems 1 and 2.

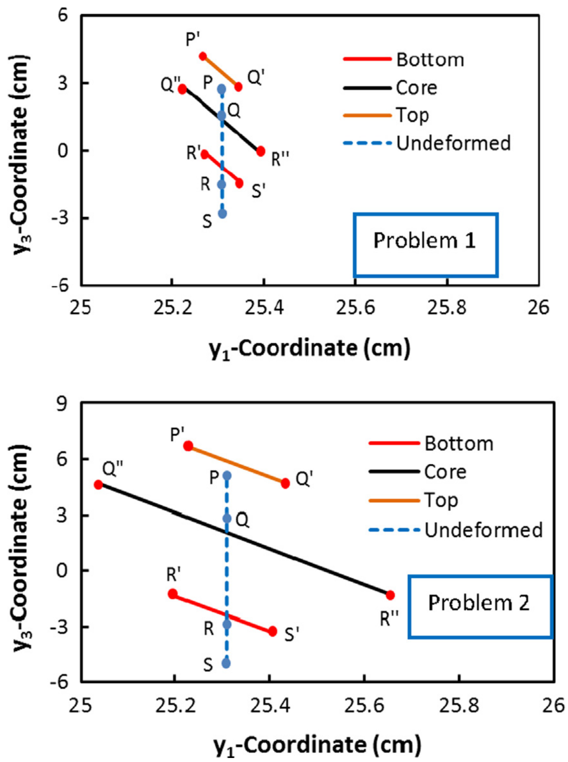

Fig. 32. Deformed configurations of a line initially perpendicular to the centroidal axis at $y_1=25.3$ cm when $t=6$ and 12 ms, respectively, for problems 1 and 2.

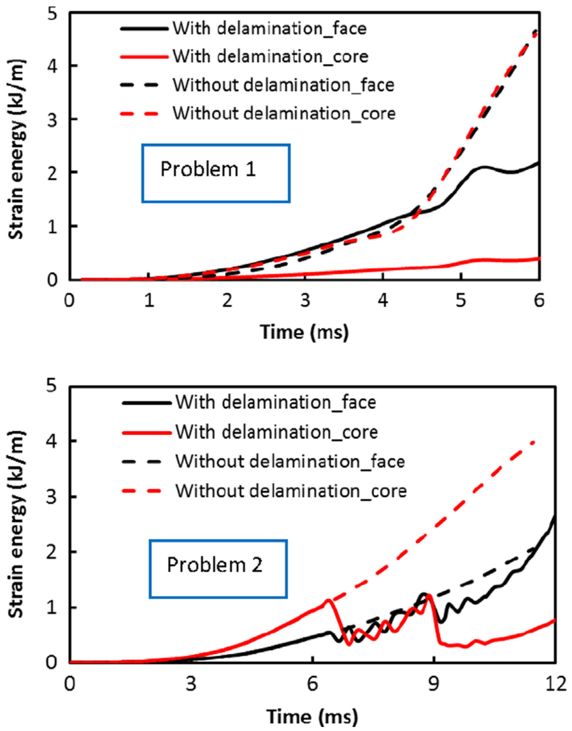

Fig. 33. Time histories of the total energy in the face sheets and the core.

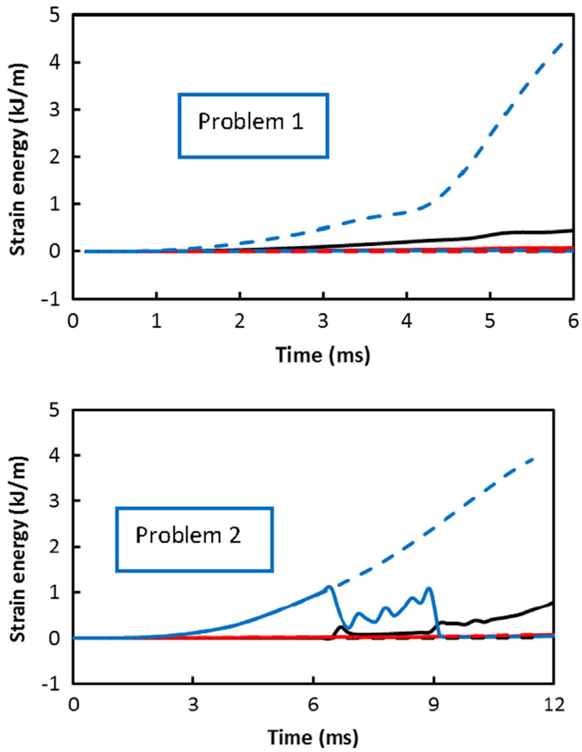

Fig. 34. Time histories of the total energy in the core due to different components of strain. The solid curves and dashed curves represent results with and without considering delamination, respectively. Black, red and blue curves represent the energy due to axial strain, transverse normal strain, and shear strain, respectively. (For interpretation of the references to color in this figure legend, the reader is referred to the web version of this article.)

In order to determine from where and when delamination initiates first, we define the separation index, ω by

$$\omega = \sqrt{\left(\frac{G_{\mathrm{I}}}{G_{\mathrm{Ic}}}\right)^2 + \left(\frac{G_{\mathrm{II}}}{G_{\mathrm{IIc}}}\right)^2}. \tag{66}$$

It equals 1 at a point when complete delamination has occurred there. In Figs. 24 and 25, we have plotted the variation of ω versus time t and y_1-coordinate on the two interfaces for problems 1 and 2, respectively. We note that ω equals the square root of the left hand side of Eq. (28), $G_{\mathrm{I}} = \int \sigma_n \, d\delta_n$, $G_{\mathrm{II}} = \int \sigma_t \, d\delta_t$ and we have taken the panel width (dimension in the y_2-direction) equal to 1 m. It is clear that the complete delamination first occurs on both interfaces at points close to the left edge or near $y_1 = 0$ at about $t = 3.6$ and 6.5 ms, respectively, for problems 1 and 2, and propagates to the right edge of the beam on both interfaces. At $t = 6$ ms, there are some regions of the panel on both interfaces for problem 1 that have not completely delaminated. However, for problem 2 the entire interfaces have been delaminated.

For problem 2, the two interfaces are delaminated at different rates with the top and the bottom interfaces completely delaminated at approximately $t = 9.1$ and 10.5 ms, respectively. The delamination rate is higher for problem 2 than that for problem 1 because there are large regions where the transverse shear stress nearly equals the critical shear stress of 3.5 MPa as shown in Fig. 26. The delamination process is unstable for problem 2 as evidenced by the sharp increases followed by arrests in the delamination lengths. Also, at $t = 9$ ms, a large portion of both interfaces near the right edge is delaminated very rapidly.

In order to delineate the mode of delamination for problems 1 and 2, we have exhibited in Figs. 27 and 28 the distribution of the SERRs, G_{I} and G_{II}, versus time t and the y_1-coordinate on the two interfaces. For both problems, the value of G_{I} is negligible as compared to that of G_{II} and the maximum values of $G_{\mathrm{I}}/G_{\mathrm{II}}$ equal 0.07 and 0.19, respectively, for problems 1 and 2. It is evident that the SERR G_{II} increases slowly after delamination initiation for problem 1. However, it increases rapidly after the delamination initiation for problem 2.

Time histories of the strain energy W_e and the kinetic energy W_k of the panel, the external work W_p done by the water slamming pressure and of the energy W_d dissipated during delamination are exhibited in Fig. 29. The energies W_e and W_k are evaluated by integrating over the panel domain the elastic energy density W (cf. Eq. (18)) and the kinetic energy density, respectively. The work W_p of water slamming pressure equals $\iint (p - p_a) H_1 d\Delta dy_1$, and the energy W_d of delamination equals $\int_{\Gamma_C} (G_{\mathrm{Ic}} + G_{\mathrm{IIc}}) H_1 \, dy_1$. Here Δ is the normal deflection of the panel, and Γ_C describes the two cohesive interfaces between the face sheets and the core. The energy dissipated during the delamination process is a miniscule part of the total work done by external forces. Discontinuities in the time histories of the elastic strain energy for problem 2 at about $t = 6.5$ and 9 ms are due to the unstable growth of delamination. The time history of the percentage difference $100(W_p - W_e - W_d - W_k)/W_p$ is shown in Fig. 30. The percentage difference is large for small values of time due to the small value of W_p that appears in the denominator, e.g., see Fig. 29. For problem 1, the percentage difference $100(W_p - W_e - W_d - W_k)/W_p$ is about 1% for $t > 2$ ms signifying that the balance of energy is well satisfied. For problem 2, the percentage difference $100(W_p - W_e - W_d - W_k)/W_p$ is about 30% after delamination has initiated. Oscillations in the error in the energy balance are due to the unstable delamination process for problem 2 as shown in Fig. 25.

In Fig. 31 we have plotted the deformed shapes of the panel at $t = 6$ and 12 ms, respectively, for problems 1 and 2. The deformed shapes are not symmetric about the mid-section because the hydroelastic pressure acting on the panel is non-uniform. The corresponding deformed configurations of a line $PQRS$ initially perpendicular to the centroidal axis are exhibited in Fig. 32. Segments PQ, QR and RS in the bottom face sheet, the core and the top face sheet are deformed, respectively, into $P'Q'$, $Q''R''$ and $R'S'$. Since the entire interfaces have been delaminated for problem 2, the panel is now composed of three separate beams connected at the edges.

Time histories of the total strain energies of the face sheets and the core are plotted in Figs. 33 and 34. For problem 1, the strain energy stored in the core is comparable to that required to deform the face sheets. For problem 2, the elastic strain energy in the core is larger than that in the face sheets. The energy absorbed in the core decreases dramatically when delamination is considered. Prior to the onset of delamination, the strain energy in the core is mainly due to transverse shear strain. However, subsequent to delamination the strain energy of deformation is mainly due to the axial strain.

5. Conclusions

Water slamming of deformable straight and curved panels has been studied using coupled boundary and finite element methods. The boundary element method (BEM) has been employed to analyze motions of the fluid, and the finite element method (FEM) coupled with a third order shear and normal deformable plate/shell theory (TSNDT) has been used to study hydroelastic problems for panels with and without considering all geometric nonlinearities, i.e., non-linear terms in the strain–displacement relations. When studying effects of geometric nonlinearities the panel material is taken to be St. Venant–Kirchhoff. The computed results for the deformable panel agree with those found by Das and Batra (2011) who used the commercial FE software LSDYNA. These suggest that the assumptions of water being incompressible and its motions being irrotational do not noticeably influence the hydroelastic effects. The consideration of geometric nonlinearities significantly increases the maximum hydrodynamic pressure experienced by the panel. However, it does not affect the traveling wave like behavior of the hydroelastic pressure acting on the panel. We have also analyzed delamination in two linear elastic sandwich panels subjected to water slamming loads. In both problems the delamination occurred at the two interfaces between the core and the face sheets due to mode-II deformations. Whereas in one problem, the delamination propagated smoothly and stably, in the other problem the delamination growth was unstable. Factors which result in stable and unstable mode-II delamination growth will be analyzed in a future study.

Acknowledgements

This work was supported by the Office of Naval Research grant N00014-11-1-0594 to Virginia Polytechnic Institute and State University with Dr. Y.D.S. Rajapakse as the Program Manager. Views expressed in the paper are those of the authors and neither of the funding agency nor of authors' Institution.

References

Abrate, S., 2011. Hull slamming. Applied Mechanics Reviews 64. (Art. no. 061003).
Anghileri, M., Spizzica, A., 1995. Experimental validation of finite element models for water impacts. In: Proceedings of the Second International Crash Users Seminar, Cranfield, UK.
Aureli, M., Prince, C., Porfiri, M., Peterson, S.D., 2010. Energy harvesting from base excitation of ionic polymer metal composites in fluid environments. Smart Materials and Structures 19. (Art. no. 015003).
Batchelor, G.K., 1967. An Introduction to Fluid Dynamics. Cambridge University Press, Cambridge, UK.
Batra, R.C., 2006. Elements of Continuum Mechanics. AIAA, Reston, VA, USA.
Batra, R.C., Liang, X.Q., 1997. Finite dynamic deformations of smart structures. Computational Mechanics 20, 427–438.
Batra, R.C., Xiao, J., 2013a. Analysis of post-buckling and delamination in laminated composite beams using CZM and layer-wise TSNDT. Composite Structures 105, 369–384.
Batra, R.C., Xiao, J., 2013b. Finite deformations of curved laminated St. Venant–Kirchhoff beam using layer-wise third order shear and normal deformable beam theory (TSNDT). Composite Structures 97, 147–164.
Battistin, D., Iafrati, A., 2003. Hydrodynamic loads during water entry of two-dimensional and axisymmetric bodies. Journal of Fluids and Structures 17, 643–664.
Berggreen, C., Simonsen, B.C., Borum, K.K., 2007. Experimental and numerical study of interface crack propagation in foam-cored sandwich beams. Journal of Composite Materials 41, 493–520.
Bisplinghoff, R.L., Doherty, C.S., 1952. Some studies of the impact of vee wedges on a water surface. Journal of the Franklin Institute 253, 547–561.
Camanho, P.P., Dávila, C.G., 2002. Mixed-mode Decohesion Finite Elements for the Simulation of Delamination in Composite Materials. NASA-Technical Paper 211737.
Causin, P., Gerbeau, J.F., Nobile, F., 2005. Added-mass effect in the design of partitioned algorithms for fluid–structure problems. Computer Methods in Applied Mechanics and Engineering 194, 4506–4527.
Charca, S., Shafiq, B., 2010. Damage assessment due to single slamming of foam core sandwich composites. Journal of Sandwich Structures and Materials 12, 97–112.
Charca, S., Shafiq, B., Just, F., 2009. Repeated slamming of sandwich composite panels on water. Journal of Sandwich Structures and Materials 11, 409–424.
Cointe, R., 1989. Two-dimensional water–solid impact. In: Proceedings of the Sixth International Offshore Mechanics and Arctic Engineering Symposium (OMAE), pp. 109–114.
Das, K., 2009. Analysis of Instabilities in Microelectromechanical Systems, and of Local Water Slamming (Ph.D. dissertation). Virginia Polytechnic Institute and State University, Blacksburg, VA.
Das, K., Batra, R.C., 2011. Local water slamming impact on sandwich composite hulls. Journal of Fluids and Structures 27, 523–551.
DIAB, 2000. Technical Manuals – Divinycell H, HT & HCP, DIAB AB, Laholm, Sweden.
Dobrovol'Skaya, Z., 1969. On some problems of similarity flow of fluid with a free surface. Journal of Fluid Mechanics 36, 805–829.
Donguy, B., Peseux, B., Gornet, L., Fontaine, E., 2001. Three-dimensional hydroelastic water entry: preliminary results. In: Proceedings of the 11th International Offshore and Polar Engineering Conference, Stavanger, Norway, pp. 324–330.
Faltinsen, O.M., 1993. Sea Loads on Ships and Offshore Structures. Cambridge University Press, Cambridge, UK.
Greco, M., 2001. A Two-dimensional Study of Green-water Loading (Ph.D. dissertation). Norwegian University of Science and Technology, Trondheim, Norwegian.
Henke, D.J., 1994. Transient deformations of plates to travelling loads with application to slamming damage. International Journal of Impact Egineering 15, 769–784.
Howison, S.D., Ockendon, J.R., Wilson, S.K., 1991. Incompressible water-entry problems at small deadrise angles. Journal of Fluid Mechanics 222, 215–230.
Hu, Z.H., He, X.D., Shi, J., Wang, R.G., Liu, H.J., 2011. Study on delamination problems of composite hull structures under slamming loads. Polymer Composites 19, 433–437.
⟨http://www.amiantit.com/media/pdf/brochures/Glass_Fibre_Reinforced_Products/files/Glass_Fibre_Reinforced_Products.pdf⟩.
Korobkin, A., 2004. Analytical models of water impact. European Journal of Applied Mathematics 15, 821–838.
Korobkin, A.A., Khabakhpasheva, T.I., 2006. Regular wave impact onto an elastic plate. Journal of Engineering Mathematics 55, 127–150.
Lin, M.C., Ho, T.Y., 1994. Water-entry for a wedge in arbitrary water depth. Engineering Analysis with Boundary Elements 14, 179–185.
Lu, C.H., He, Y.S., Wu, G.X., 2000. Coupled analysis of nonlinear interaction between fluid and structure during impact. Journal of Fluids and Structures 14, 127–146.
Mei, X., Liu, Y., Yue, D.K.P., 1999. On the water impact of general two-dimensional sections. Applied Ocean Research 21, 1–15.
Miloh, T., 1991a. On the initial-stage slamming of a rigid sphere in a vertical water entry. Applied Ocean Research 13, 43–48.
Miloh, T., 1991b. On the oblique water-entry problem of a rigid sphere. Journal of Engineering Mathematics 25, 77–92.
Nila, A., Vanlanduit, S., Vepa, S., Van Nuffel, D., Van Paepegem, W., Degroote, J., Vierendeels, J., 2012. High speed particle image velocimetry measurements during water entry of rigid and deformable bodies. In: Proceedings of the 16th International Symposium on Applications of Laser Techniques to Fluid Mechanics, Lisbon, Portugal, pp. 1–11.
Oger, G., Doring, M., Alessandrini, B., Ferrant, P., 2006. Two-dimensional SPH simulations of wedge water entries. Journal of Computational Physics 213, 803–822.
Panciroli, R., Abrate, S., Minak, G., 2013. Dynamic response of flexible wedges entering the water. Composite Structures 99, 163–171.
Panciroli, R., Abrate, S., Minak, G., Zucchelli, A., 2012. Hydroelasticity in water-entry problems: comparison between experimental and SPH results. Composite Structures 94, 532–539.
París, F., Cañas, J., 1997. Boundary Element Method: Fundamentals and Applications. Oxford University Press, New York.
Piro, D.J., Maki, K.J., 2013. Hydroelastic analysis of bodies that enter and exit water. Journal of Fluids and Structures 37, 134–150.
Qin, Z., Batra, R.C., 2009. Local slamming impact of sandwich composite hulls. International Journal of Solids and Structures 46, 2011–2035.
Ray, M.C., Batra, R.C., 2013. Transient hydroelastic analysis of sandwich beams subjected to slamming in water. Thin-Walled Structures 72, 206–216.

Saada, A.S., 1993. Elasticity: Theory and Applications. Krieger (Malabar, FL).
Schnitzer, E., Hathaway, M.E., 1953. Estimation of Hydrodynamic Impact Loads and Pressure Distributions on Bodies Approximating Elliptical Cylinders with Special Reference to Water Landings of Helicopters. National Advisory Committee for Aeronautics.
Seddon, C.M., Moatamedi, M., 2006. Review of water entry with applications to aerospace structures. International Journal of Impact Engineering 32, 1045–1067.
Sedov, L., 1934. The Impact of a Solid Body Floating on the Surface of an Incompressible Fluid. CAHI Report 187, Moscow.
Shiffman, M., Spencer, D., 1951. The force of impact on a cone striking a water surface (vertical entry). Communications on Pure and Applied Mathematics 4, 379–417.
Shiffman, M., Spencer, D.C., 1945. The Force of Impact on a Sphere Striking a Water Surface. NYAMP, Report 42. New York University Courant Institute of Mathematical Sciences, New York.
Stenius, I., Rosén, A., Kuttenkeuler, J., 2006. Explicit FE-modelling of fluid–structure interaction in hull-water impacts. International Shipbuilding Progress 53, 103–121.
Stenius, I., Rosén, A., Kuttenkeuler, J., 2011. Hydroelastic interaction in panel-water impacts of high-speed craft. Ocean Engineering 38, 371–381.
Sun, H., 2007. A Boundary Element Method Applied to Strongly Nonlinear Wave–body Interaction Problems (Ph.D. Dissertation). Norwegian University of Science and Technology, Trondheim, Norwegian.
Sun, H., Faltinsen, O.M., 2006. Water impact of horizontal circular cylinders and cylindrical shells. Applied Ocean Research 28, 299–311.
Sun, H., Faltinsen, O.M., 2009. Water entry of a bow-flare ship section with roll angle. Journal of Marine Science and Technology 14, 69–79.
Szebehely, V., 1959. Hydrodynamic impact. Applied Mechanics Reviews 12, 297–300.
Szebehely, V.G., Basin, E.D.T.M., 1954. Progress in theoretical and experimental studies of ship slamming. In: Johnson, J.W. (Ed.), Proceedings of the First Conference on Ships and Waves, Hoboken, NJ, USA, pp. 230–250.
Trilling, L., 1950. The impact of a body on a water surface at an arbitrary angle. Journal of Applied Physics 21, 161–170.
van Paepegem, W., Blommaert, C., De Baere, I., Degrieck, J., De Backer, G., De Rouck, J., Degroote, J., Vierendeels, J., Matthys, S., Taerwe, L., 2011. Slamming wave impact of a composite buoy for wave energy applications: design and large-scale testing. Polymer Composites 32, 700–713.
von Karman, T., 1929. The Impact on Seaplane Floats During Landing. National Advisory Committee for Aeronautics, Technical Note Number 321.
Wagner, H., 1932. Über Stoß-und Gleitvorgänge an der Oberfläche von Flüssigkeiten. ZAMM-Journal of Applied Mathematics and Mechanics/Zeitschrift für Angewandte Mathematik und Mechanik 12, 193–215.
Wu, G.X., 1998. Hydrodynamic force on a rigid body during impact with liquid. Journal of Fluids and Structures 12, 549–559.
Wu, G.X., Sun, H., He, Y.S., 2004. Numerical simulation and experimental study of water entry of a wedge in free fall motion. Journal of Fluids and Structures 19, 277–289.
Wu, G.X., Taylor, R.E., 1996. Transient motion of a floating body in steep water waves. In: Proceedings of the 11th Workshop on Water Waves and Floating Bodies, Hamburg, Germany.
Wu, G.X., Taylor, R.E., 2003. The coupled finite element and boundary element analysis of nonlinear interactions between waves and bodies. Ocean Engineering 30, 387–400.
Xiao, J., Batra, R.C., 2012. Local water slamming of curved rigid hulls. International Journal of Multiphysics 6, 305–339.
Xu, G.D., Duan, W.Y., Wu, G.X., 2010. Simulation of water entry of a wedge through free fall in three degrees of freedom. Proceedings of the Royal Society A: Mathematical, Physical and Engineering Science 466, 2219–2239.
Yettou, E.M., Desrochers, A., Champoux, Y., 2007. A new analytical model for pressure estimation of symmetrical water impact of a rigid wedge at variable velocities. Journal of Fluids and Structures 23, 501–522.
Young, Y.L., 2007. Time-dependent hydroelastic analysis of cavitating propulsors. Journal of Fluids and Structures 23, 269–295.
Yu, Y.T., 1945. Virtual masses of rectangular plates and parallelepipeds in water. Journal of Applied Physics 16, 724–729.
Zenkert, D., 1991. Strength of sandwich beams with interface debondings. Composite Structures 17, 331–350.
Zhao, R., Faltinsen, O., 1993. Water entry of two-dimensional bodies. Journal of Fluid Mechanics 246, 593–612.
Zhao, R., Faltinsen, O., Aarsnes, J., 1997. Water entry of arbitrary two-dimensional sections with and without flow separation. In: Proceedings of the Twenty-First Symposium on Naval Hydrodynamics of National Research Council. The National Academies Press, Washington, DC, pp. 408–423.